LUND UNIVERSITY

Gradient-based optimization of non-linear structures and materials

Dalklint, Anna

2023

LUNDS UNIVERSITET

GRADIENT-BASED OPTIMIZATION OF NON-LINEAR STRUCTURES AND MATERIALS

ANNA DALKLINT

Solid Mechanics

Doctoral Thesis

Department of Construction Sciences
Solid Mechanics

ISRN LUTFD2/TFHF-23/1067-SE (1-216)
ISBN: 978-91-8039-544-1 (print)
ISBN: 978-91-8039-545-8 (pdf)

Gradient-based optimization of non-linear structures and materials

Doctoral Thesis by

Anna Dalklint

Printed by Media-Tryck AB, Lund, Sweden

Media-Tryck is a Nordic Swan Ecolabel certified provider of printed material. Read more about our environmental work at www.mediatryck.lu.se

MADE IN SWEDEN

For information, address:
Division of Solid Mechanics, Lund University, Box 118, SE-221 00 Lund, Sweden
Homepage: http://www.solid.lth.se

Till minne av Carin Larsson

Preface

During the last circa five years, I have been granted the pleasure of conducting research at the Division of Solid Mechanics, Lund University. As a result, I can now proudly present this thesis. Of course, there are plenty of people who have accompanied me along this journey, and I would like to take this opportunity to express my gratitude to those. First and foremost, I would like to thank my supervisor (aka academic dad), Prof. Mathias Wallin, whose guidance and enthusiasm has been invaluable during this time. I would also like to give special thanks to Prof. Daniel Tortorelli, who has always thoroughly inspected my work and provided helpful insights. Along this line, I thank the rest of the optimization team at Lawrence Livermore National Laboratory, who let me stay for a summer internship, and Dr. Felipe Fernandez, who helped me find housing and showed me California. I also thank Prof. Matti Ristinmaa, Dr. Seth Watts and Prof. Katia Bertoldi for their support in this thesis. Special thanks to Skånska Ingenjörsklubben and SAAB for granting me scholarships.

Of course, I must thank all past and current colleagues at the division for fruitful coffee breaks and fun times outside the office. Special thanks to Dr. Niklas Ivarsson, for being a splendid mentor and for insightful discussions on topology optimization. I am grateful for being part of the "topopt group" at the division, where both technical discussions and afterworks are always a delight. The teachers I had in younger years deserve recognition for their dedicated work, and for inspiring me to do my best. Thanks to all my dear friends, who will always have a special place in my heart. I wish to express my deepest gratitude to my family, for their unconditional love and support. Lastly, I thank my beloved husband, Edvin, for your unrivaled ability to make me happy.

Lund, December 2022
Anna Dalklint

Abstract

Gradient-based optimization is a potent tool in many design processes today. It is particularly useful in industries where weight considerations are crucial, such as aerospace, but can also be exploited in for example civil engineering applications to reduce the material use and thereby the environmental impact. With the advent of advanced manufacture methods, it even possesses the potential to design novel materials with enhanced properties that naturally occurring materials lack. Unfortunately, most research on the subject often limits itself to linear problems, wherefore the optimization's utility in solving intricate non-linear problems is still comparatively rudimentary. The aim of this thesis is therefore to investigate gradient-based optimization of various non-linear structural problems, while addressing their inherent numerical and modeling complexities.

This thesis contains an introduction to gradient-based optimization of non-linear structures and materials, involving both shape and topology optimization. To start, the governing equations of the macroscopic and microscopic problems are described. A multi-scale framework which details the transition between the scales is defined. A substantial part of the thesis is dedicated to eigenvalue problems in topology optimization, and the numerical issues that they accompany. Specifically, the effects of finite deformations on the topology optimized design taking into account eigenfrequencies, structural stability or elastic wave propagation are scrutinized. A fictitious domain approach to topology optimization is employed, wherein void regions are modeled via an ersatz material with low stiffness. Unfortunately, this brings about artificial eigenmodes and convergence problems in the finite element analyzes. Two methods which deal with both of the aforementioned problems are proposed, and their efficacy is illustrated via several numerical examples. The use of shape optimization to post-process topology optimized designs is investigated for problems where accurate boundary descriptions are crucial to capture the physics, as is the case in contact problems. To take this concept further, a simultaneous topology and shape optimization method is proposed, which allows parts of the structural boundaries to be modeled exactly up to numerical precision. This approach is proven to be especially useful in the design of pressure-driven soft robots.

Populärvetenskaplig sammanfattning

Vid tillverkning av strukturella komponenter är mängden och typen av tillgängligt material ofta begränsat i den mån att komponenten inte får vara för tung och dyr. Samtidigt skall komponenten uppfylla sitt ändamål, som exempelvis att kunna bära en viss last utan att deformeras för mycket, eller att inte uppnå resonans när den utsätts för vibrationer inom specifika frekvensspann. Traditionellt utgörs en designprocess utav iterativ utvärdering av inkrementellt förbättrade designer som tas fram baserat på mänsklig intuition och erfarenhet. Förutom att den här typen av designprocess är tidskrävande och dyr, så garanterar den ej att den slutgiltiga designen är optimal.

Med hjälp av matematiska optimeringsmetoder förenklas sökandet efter optimal design, samtidigt som designprocessen effektiviseras. En tidig typ av optimering var formoptimering, där strukturens ränder förflyttas för att uppnå en förbättring av dess egenskaper. För att möjliggöra större förändringar av strukturens geometri utvecklades senare topologioptimering, där ändringar gällande form, tjocklek samt sammankopplingar mellan olika beståndsdelar tillåts. Lösningen till ett matematiskt optimeringsproblem utgör en konceptuell design som är optimerad i förhållande till uttryckta önskemål.

För att lösa ett visst optimeringsproblem, måste strukturens hållfasthet utvärderas. I vissa fall kan även andra egenskaper såsom egenfrekvenser och stabilitet behöva utredas. För att beskriva det fysikaliska systemet införs vissa antaganden, som exempelvis små töjningar och linjärelastisk materialrespons, vilka avsevärt förenklar lösningen av de styrande differentialekvationerna. Tyvärr begränsar även dessa antaganden användningen av optimeringsmetoderna, då många strukturer och material i verkligheten beter sig högst olinjärt.

I den här avhandlingen modelleras både struktur och material med hjälp av avancerade olinjära teorier och metoder. Avhandlingen behandlar optimering av strukturella problem där egenvärdesproblem uppstår, såsom är fallet då hänsyn tas till egenfrekvenser, stabilitet eller vågutbredning. De numeriska metoder som krävs för att lösa egenvärdesproblem i topologioptimering utvecklas och analyseras. Här utröns även hur egenvärden påverkas av yttre last, det vill säga spänningar i strukturen. Resultaten visar på en tydlig inverkan av pålagda krafter, vilket leder till stora förändringar av den optimerade designen jämfört med om antaganden om linjäritet antas.

En annan del av avhandlingen behandlar det ytterst olinjära fenomenet kontakt i kombination med topologioptimering. Så kallade metamaterial, det vill säga material med egenskaper som inte existerar i naturligt förekommande material, designas vilka utnyttjar kontakt som en olinjär mekanism. Här genomförs även rigorösa post-processerings analyser, där designen extraheras och dess egenskaper utvärderas.

Slutligen presenteras en optimeringsmetod som utför form- och topologioptimering samtidigt. Metoden visar sig vara mycket användbar i fall då randrepresentation är av stor betydelse, som till exempel vid optimering av tryckdrivna robotar. Den här typen av robotar, som ofta benämns mjuka robotar, har nyligen fått stor uppmärksamhet på grund av deras låga tillverkningskostnad och stora mångsidighet. Olinjär antaganden krävs för att korrekt modellera robotarnas rörelse, då ofta stora töjningar och hyperelastiska material såsom gummi är involverade.

List of appended papers

This doctoral thesis is based upon the following manuscripts:

Paper A
Anna Dalklint, Mathias Wallin and Daniel Tortorelli
Eigenfrequency constrained topology optimization of finite strain hyperelastic structures
Structural and Multidisciplinary Optimization 61.6 (2020): 2577-2594

Paper B
Anna Dalklint, Mathias Wallin and Daniel Tortorelli
Structural stability and artificial buckling modes in topology optimization
Structural and Multidisciplinary Optimization 64.4 (2021): 1751-1763

Paper C
Anna Dalklint, Mathias Wallin, Katia Bertoldi and Daniel Tortorelli,
Tunable phononic bandgap materials designed via topology optimization
Journal of the Mechanics and Physics of Solids 163 (2022): 104849

Paper D
Anna Dalklint, Filip Sjövall, Mathias Wallin, Seth Watts and Daniel Tortorelli
Computational design of metamaterials with self contact
Submitted for publication

Paper E
Anna Dalklint, Mathias Wallin, Katia Bertoldi and Daniel Tortorelli
Simultaneous shape and topology optimization of inflatable soft robots
To be submitted for publication

Own Contribution
The author of this thesis has taken the main responsibility for the preparation and writing of all appended papers. The numerical models have been developed in collaboration with the co-authors, whereas the implementation of the models has been conducted by the main author. In Paper D, the post-processing analyzes have been performed in collaboration with Filip Sjövall.

List of papers not included in this thesis

Mathias Wallin, Anna Dalklint and Daniel Tortorelli
Topology optimization of bistable elastic structures - An application to logic gates
Computer Methods in Applied Mechanics and Engineering 383 (2021): 113912

Vilmer Dahlberg, Anna Dalklint, Oded Amir and Mathias Wallin
Efficient buckling constrained topology optimization using reduced order modeling
Submitted for publication

Contents

1 Introduction

The traditional design process of structural components involves heuristic techniques which iteratively construct and evaluate conceptual designs based on human intuition and experience. Although this process has proven its usefulness over the last centuries, it is certainly inefficient and does not guarantee convergence towards optimal designs. The modern scientific development has further raised the demand for increasingly efficient state-of-the-art design processes, as advanced components involving multiple length-scales and branches of physics are needed. Here, computational design tools based on mathematical programming excel, displaying great efficiency and ability to yield (at least local) optima in the design space.

An example of such a tool is gradient-based structural optimization. The method was originally limited to the design of linear elastic load-bearing structures, typically with the aim to maximize the stiffness-to-mass ratio. Nowadays, gradient-based optimization has proven applicable in design problems involving various types of physics, such as photonics (Jensen and Sigmund (2011)), fluids (Borrvall and Petersson (2003)) and electromagnetics (Dyck and Lowther (1996)). Indeed, the method can even be used to design so-called meta-materials, with physical properties that do not typically occur in materials found in nature, like negative thermal expansion (Sigmund and Torquato (1997)) or negative Poisson's ratio (Larsen et al. (1997)).

A structural optimization problem is typically posed as a shape or topology optimization problem. The former approach parametrizes the design's boundaries, and morphs the design into its optimized configuration. The latter approach instead quantifies the material distribution in the design domain via a density field, which allows immense transformations of the design's morphology, but deteriorates the precision in the modeling of the design's boundaries. Therefore, shape optimization is the obvious candidate for improving structures with predefined topologies, whereas topology optimization is superior when permitting greater design freedom.

The early research on structural optimization was restricted to analytical methods. A famous example is the work by Michell (1904), who presented optimized linear elastic frame structures. With the advent of numerical methods such as the finite element method, more advanced optimization methods could be developed. For example, the seminal works by Zienkiewicz and Campbell (1973) and Bendsøe and Kikuchi (1988) pioneered the nodal-based shape optimization and the density-based topology optimization, respectively. Modern research on structural optimization address e.g. the expansion to large scale problems (Alexandersen et al. (2016), Aage et al. (2017)), multi-physics (Zhao and Zhang (2022), Kang and James (2022)), manufacturing constraints (Mhapsekar et al. (2018), Zhang and Cheng (2020)) and irreversible processes (Li et al. (2017), Ivarsson et al. (2018), Carstensen et al. (2022)).

Another field of research which currently is devoted much attention is the design of non-linear hyperelastic mechanical structures and materials. The inherent reversibility of such systems can be exploited to create applications with exotic behaviors, such as tunable Poisson's ratio (Bertoldi et al. (2010)), tunable phononic bandgaps (Bertoldi and Boyce (2008)) or programmable materials (Florijn et al. (2014)). Frenzel et al. (2016) utilize buckling instabilities to design reusable shock absorbers. An interesting application is the characterization and design of soft robots, which typically requires a model which captures the finite deformation of hyperelastic elastomers such as rubber, cf. Rus and Tolley (2015) and Paper E.

Gradient-based optimization can be used as a systematic tool to produce designs which exhibit the aforementioned behaviors. Early contributions to the structural optimization of non-linear hyperelastic mechanical problems include Buhl et al. (2000) and Bruns and Tortorelli (2001), whereby stiff structures are sought. Wallin et al. (2018) illustrate that the definition of stiffness is non-unique for non-linear problems, i.e. that structures that minimize the displacement for a given load might in fact lack "true" stiffness in the sense of being instable in that equilibrium position. Buckling objectives in topology optimization are considered by e.g. Kemmler et al. (2005), Lindgaard and Dahl (2013) and Dalklint et al. (2021) (Paper B), wherein eigenvalue problems are solved to identify the critical instable equilibrium positions. The solutions to eigenvalue problems are also needed in optimization formulations involving vibration analyzes (Yoon (2010a), Dalklint et al. (2020) (Paper A)). Examples of systematic design of hyperelastic meta-materials include the topology optimization of programmable Poisson's ratio materials (Wang (2018)), tunable phononic crystal materials (Dalklint et al. (2022) (Paper C)), energy dissipating lattice structures (Deng et al. (2020)) and materials which utilize self-contact to obtain a prescribed macroscopic response (Paper D).

1.1 Research aim

This thesis presents a theoretical and computational framework which designs non-linear structures and materials using gradient-based optimization. The aim of the research is to expand the applicability of the state-of-the-art gradient-based optimization to various hyperelastic engineering problems, including both modeling and numerical aspects.

2 Governing equations

This section introduces the balance, kinematical and constitutive equations that govern the non-linear physical systems covered in this thesis. The concepts of *macroscopic* and *microscopic* scales are distinguished. Here, the terminology of the microscopic scale refers to systems of characteristic lengths much smaller than that of the macroscopic continuum, i.e. is not necessarily microscopic in the conventional sense. For example, the multiscale model of concrete might utilize a microscale in the order of centimeters to represent the cement and aggregate composite. Papers A, B and E considers the modeling of macroscopic structures, whereas Papers C and D involves structures at the microscopic scale.

2.1 Macroscopic relations

To consider finite deformations, the undeformed, reference configuration $\Omega \in \mathbb{R}^2$, and the deformed, current configuration $\Omega_c \in \mathbb{R}^2$ are distinguished[1], cf. Fig. 2.1. The transformation of a material point $\boldsymbol{X} \in \Omega$ to $\boldsymbol{x} \in \Omega_c$ at time $t > 0$ is described by a smooth mapping $\boldsymbol{x}(\boldsymbol{X}, t) = \boldsymbol{\varphi}(\boldsymbol{X}, t) = \boldsymbol{X} + \boldsymbol{u}(\boldsymbol{X}, t)$, where $\boldsymbol{u} : \Omega \to \mathbb{R}^2$ denotes the displacement field. The local deformation is described by the deformation gradient

$$\boldsymbol{F}(\boldsymbol{X}, t) = \boldsymbol{\nabla}\boldsymbol{\varphi}(\boldsymbol{X}, t) = \mathsf{1} + \boldsymbol{\nabla}\boldsymbol{u}(\boldsymbol{X}, t), \tag{2.1}$$

where $\boldsymbol{\nabla}$ is the material gradient operator on Ω and $\mathsf{1}$ is the second order identity tensor. The Jacobian representing the local volumetric change is $J = \det(\boldsymbol{F})$. The local deformation is further described by the right Cauchy-Green deformation tensor $\boldsymbol{C} = \boldsymbol{F}^T \cdot \boldsymbol{F}$ and the Green-Lagrange strain tensor $\boldsymbol{E} = \frac{1}{2}(\boldsymbol{C} - \mathsf{1})$. For later purposes, the linearized strain $\boldsymbol{\epsilon} = \frac{1}{2}((\boldsymbol{\nabla}\boldsymbol{u})^T + \boldsymbol{\nabla}\boldsymbol{u})$ is also introduced.

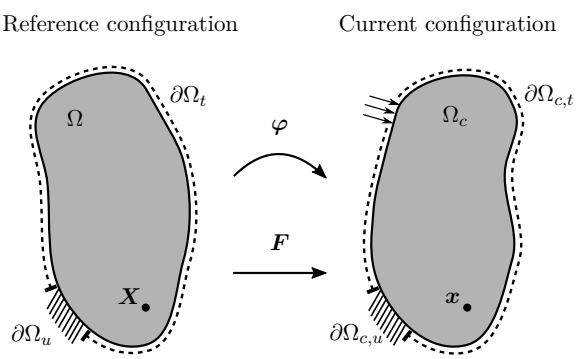

Fig. 2.1: The deformation of a macroscopic body.

In absence of body forces, the governing equations of motion of a compressible macroscopic body

[1]Without loss of generality, the physical space is restricted to two dimensions.

are

$$\begin{aligned} \boldsymbol{\nabla} \cdot \boldsymbol{P} &= \rho \frac{\partial^2 \boldsymbol{u}}{\partial t^2} \ \text{ in } \ \Omega, \\ \boldsymbol{P} \cdot \boldsymbol{n} &= \hat{\boldsymbol{t}} \ \text{ at } \ \partial\Omega_t, \\ \boldsymbol{u} &= \hat{\boldsymbol{u}} \ \text{ at } \ \partial\Omega_u, \end{aligned} \tag{2.2}$$

where $\boldsymbol{P}$ is the macroscopic first Piola-Kirchhoff stress tensor, $\rho > 0$ is the mass density in the reference configuration and the boundary $\partial\Omega$ with unit normal $\boldsymbol{n}$, is decomposed into the disjoint sets $\partial\Omega_t$ and $\partial\Omega_u$, over which the traction $\boldsymbol{t} = \hat{\boldsymbol{t}}$ and the displacement $\boldsymbol{u} = \hat{\boldsymbol{u}}$, are prescribed, respectively. The equilibrium configurations of Ω are also described by those $\boldsymbol{u} \in \{\boldsymbol{u} \in H^1 : \boldsymbol{u}(\boldsymbol{X}, t) = \hat{\boldsymbol{u}} \text{ for } \boldsymbol{X} \in \partial\Omega_u\}$, which satisfy the weak formulation of (2.2)

$$\delta r(\boldsymbol{u}; \delta\boldsymbol{u}) := \int_\Omega \rho \frac{\partial^2 \boldsymbol{u}}{\partial t^2} \cdot \delta\boldsymbol{u} \, dV + \int_\Omega \boldsymbol{P} : \delta\boldsymbol{F} \, dV - \int_{\partial\Omega_t} \hat{\boldsymbol{t}} \cdot \delta\boldsymbol{u} \, dV = 0, \tag{2.3}$$

for all smooth admissible virtual displacements $\delta\boldsymbol{u}$, where $\delta(\,\cdot\,)$ is the variational operator and H^1 is a Hilbert space. Note that (2.2) or (2.3) readily are reduced to quasi-static conditions by neglecting the inertial effects.

2.1.1 Constitutive model

To solve the (2.2) equations of motion, or equivalently the weak form (2.3), a constitutive model which describes the relationship between the stresses and the deformation is required. The choice of constitutive model ultimately depends upon what type of material that constitutes Ω, in combination with the specific conditions, e.g. load magnitude, the body is subjected to.

Herein, isotropic hyperelasticity is assumed when solving macroscopic boundary value problems. Under conservative quasi-static loading, this assumption presumes the existence of an energy potential

$$\Pi(\boldsymbol{u}) = \Pi_{int} - \Pi_{ext} = \int_\Omega W \, dV - \int_{\partial\Omega} \boldsymbol{t} \cdot \boldsymbol{u} \, dV, \tag{2.4}$$

where $W = W(\boldsymbol{\nabla}\boldsymbol{u})$ is the load history independent strain energy density. The stationarity of (2.4) yields the weak formulation (2.3), where the first Piola-Kirchhoff stress tensor is derived from W as

$$\boldsymbol{P} = \frac{\partial W}{\partial \boldsymbol{F}}. \tag{2.5}$$

For later use, the Cauchy stress tensor is $\boldsymbol{\sigma} = \frac{1}{J}\boldsymbol{P} \cdot \boldsymbol{F}^T$ and the second Piola-Kirchhoff stress tensor is $\boldsymbol{S} = \boldsymbol{F}^{-1} \cdot \boldsymbol{P}$. Also, the incremental elasticity tensor is

$$\boldsymbol{L} = \frac{\partial^2 W}{\partial \boldsymbol{F} \partial \boldsymbol{F}}. \tag{2.6}$$

The elastic strain energy density, W, is, unless stated otherwise, stated in the form of a compressible neo-Hookean model

$$W = \frac{1}{4} K \left((J^2 - 1) - \ln\left(J^2\right) \right) + \frac{1}{2} G \left(J^{-2/3} \text{tr}(\boldsymbol{F}^T \cdot \boldsymbol{F}) - 3 \right), \tag{2.7}$$

where K and G correspond to the bulk and shear moduli in the limit of infinitesimal strain. Other hyperelastic models appear in e.g. Holzapfel (2002).

2.1.2 Total Lagrangian finite element formulation

The boundary value problem (2.2) is solved using a total Lagrangian approach, wherefore the associated weak form (2.3) is discretize via a finite element (FE) mesh over the reference configuration, Ω. A Galerkin approach (Bathe (2006)) is utilized, wherefore both physical and variational displacement fields are approximated using element polynomial shape functions N, e.g. $\boldsymbol{u}(\boldsymbol{X},t) \approx \mathsf{N}(\boldsymbol{X})\mathsf{u}_e(t)$ and $\delta\boldsymbol{u}(\boldsymbol{X}) \approx \mathsf{N}(\boldsymbol{X})\delta\mathsf{u}_e$, where $\mathsf{u}_e(t)$ and $\delta\mathsf{u}_e$ are element nodal coefficients. The second derivative of u with respect to t gives the approximative acceleration $\frac{\partial^2\boldsymbol{u}(\boldsymbol{X})}{\partial t^2} \approx \mathsf{N}(\boldsymbol{X})\ddot{\mathsf{u}}_e(t)$.

Using the arbitrariness of the virtual nodal displacement and the finite element interpolations in (2.3), yields the discretized residual

$$\mathsf{r} = \mathsf{M}\ddot{\mathsf{u}} + \mathsf{F}_{int} - \mathsf{F}_{ext} = \mathbf{0}, \tag{2.8}$$

where the mass matrix $\mathsf{M} = \sum\!\!\!\!\!\!\int_{\Omega^e} \rho\mathsf{N}^T\mathsf{N}\,dV$, internal force vector $\mathsf{F}_{int} = \sum\!\!\!\!\!\!\int_{\Omega^e} (\boldsymbol{\nabla}\mathsf{N})^T\,\mathsf{P}\,dV$, and external force vector $\mathsf{F}_{ext} = \sum\!\!\!\!\!\!\int_{\partial\Omega_t^e} \mathsf{N}^T\hat{\mathsf{t}}\,dS$ are introduced. Here, $\sum\!\!\!\!\!\!\int$ denotes the finite element assembly operator and $\mathsf{P} = [P_{11},\, P_{12},\, P_{21},\, P_{22}]^T$. Typically, the external load is assumed to be independent of the displacement, a situation referred to as "dead" loading. In this case, it is convenient to assume $\mathsf{F}_{ext} = \lambda\mathsf{l}$, where $\lambda \in \mathbb{R}$ is the load scaling factor and $\mathsf{l} \in \mathbb{R}^n$ describes the load direction.

To solve (2.8), a Newton-Raphson iterative procedure could be utilized, wherein the truncated Taylor series expansion

$$\mathsf{r}(\mathsf{u} + d\mathsf{u}) \approx \mathsf{r}(\mathsf{u}) + \frac{\partial\mathsf{r}(\mathsf{u})}{\partial\mathsf{u}}d\mathsf{u} = \mathbf{0}, \tag{2.9}$$

is required. In (2.9), the Hessian of the potential energy appears, i.e. the tangent stiffness matrix

$$\mathsf{K} = \frac{\partial\mathsf{r}}{\partial\mathsf{u}} = \sum\!\!\!\!\!\!\int_{\Omega^e} (\boldsymbol{\nabla}\mathsf{N})^T\,\mathsf{L}\,(\boldsymbol{\nabla}\mathsf{N})\;dV, \tag{2.10}$$

where L is the incremental elasticity tensor in Voigt notation.

2.2 Microscopic relations

Let us now consider a macroscopic body Ω, which consists of a heterogeneous material with a hitherto unknown constitutive behavior. To predict the mechanical behavior of the material at each macroscopic material point $\boldsymbol{X} \in \Omega$, *homogenization* can be employed, wherein the material's stress and strain fields are obtained as volume averages over a representative unit cell $\Omega^\mu \in \mathbb{R}^2$. It is assumed that the microstructure is at least locally periodic, cf. Fig. 2.2, and that the assumption of separation of length scales holds, wherefore $|\Omega^\mu| \ll |\Omega|$, where $|\cdot|$ denotes the area. Without loss of generality, rectangular unit cells with primitive lattice vectors $\boldsymbol{A}_1 = a_1\boldsymbol{e}_1$ and $\boldsymbol{A}_2 = a_2\boldsymbol{e}_2$ are considered, where $\boldsymbol{e}_1$ and $\boldsymbol{e}_2$ are the orthonormal basis vectors and $(a_1, a_2) \in (\mathbb{R} \times \mathbb{R})$. The unit cell boundary $\partial\Omega^\mu$ with outward unit normal $\boldsymbol{n}$ is decomposed in the disjoint sets $\partial\Omega^{\mu+} = \partial\Omega^{\mu1+} \cup \partial\Omega^{\mu2+}$ and $\partial\Omega^{\mu-} = \partial\Omega^{\mu1-} \cup \partial\Omega^{\mu2-}$, containing material points on opposite boundaries, cf. Fig. 2.2.

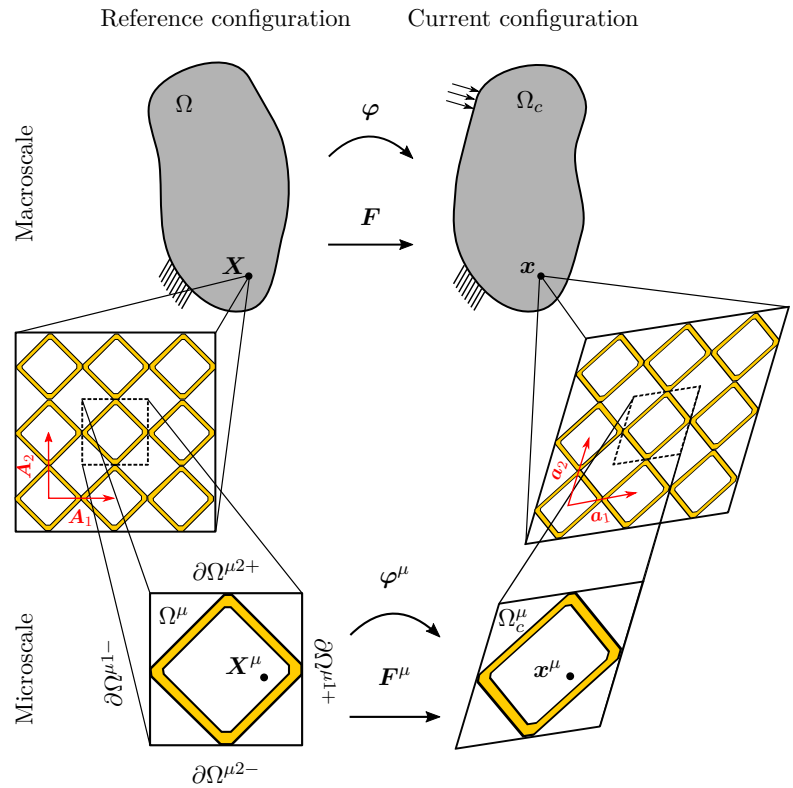

Fig. 2.2: The deformation of a macroscopic body and its effect on the periodic microstructure.

It is assumed that the macroscopic deformation $\boldsymbol{F}$ drives the microscopic displacement field $\boldsymbol{u}^\mu : \Omega \to \mathbb{R}^2$, such that each microscopic material point $\boldsymbol{X}^\mu \in \Omega^\mu$, is displaced to the position $\boldsymbol{x}^\mu(\boldsymbol{X}, t) = \boldsymbol{\varphi}^\mu(\boldsymbol{X}, t) = \boldsymbol{u}^\mu(\boldsymbol{X}, t) + \boldsymbol{X}^\mu \in \Omega^\mu_c$, where

$$\boldsymbol{u}^\mu(\boldsymbol{X}^\mu, t) = (\boldsymbol{F}(t) - \mathbf{1}) \cdot \boldsymbol{X}^\mu + \boldsymbol{u}^F(\boldsymbol{X}^\mu, t), \tag{2.11}$$

$\boldsymbol{F}$ is uniform over Ω^μ due to the separation of scales and $\boldsymbol{u}^F(\boldsymbol{X}^\mu, t)$ is the heterogeneous displacement fluctuation field, cf. Saeb et al. (2016). The microscopic deformation gradient $\boldsymbol{F}^\mu$ is derived from (2.11)

$$\boldsymbol{F}^\mu(\boldsymbol{X}^\mu, t) = \boldsymbol{\nabla}^\mu \boldsymbol{\varphi}^\mu(\boldsymbol{X}^\mu, t) = \mathbf{1} + \boldsymbol{\nabla}^\mu \boldsymbol{u}^\mu(\boldsymbol{X}^\mu, t) = \boldsymbol{F}(t) + \boldsymbol{\nabla}^\mu \boldsymbol{u}^F(\boldsymbol{X}^\mu, t), \tag{2.12}$$

where $\boldsymbol{\nabla}^\mu$ is the gradient operator with respect to the microscopic reference coordinates $\boldsymbol{X}^\mu$. Similarly to the macroscopic problem (2.2), it is assumed that the microscopic problem is in quasi-static force equilibrium, i.e.

$$\boldsymbol{\nabla}^\mu \cdot \boldsymbol{P}^\mu = \mathbf{0} \ \text{ in } \ \Omega^\mu, \tag{2.13}$$

assuming negligible body forces due to the separation of scales. In the above, the hyperelastic assumption necessitates that $\boldsymbol{P}^\mu = \frac{\partial W^\mu}{\partial \boldsymbol{F}^\mu}$, where W^μ is the microscopic energy function.

The above equations of motion require suitable boundary conditions. To this end, the microscopic displacement field is postulated to satisfy the kinematical homogenization, or averaging, relations

$$\boldsymbol{u} = \frac{1}{|\Omega^\mu|}\int_{\Omega^\mu} \boldsymbol{u}^\mu \, dV, \tag{2.14}$$

and

$$\boldsymbol{F} = \frac{1}{|\Omega^\mu|}\int_{\Omega^\mu} \boldsymbol{F}^\mu \, dV = \mathbf{1} + \frac{1}{|\Omega^\mu|}\int_{\Omega^\mu} \boldsymbol{\nabla}^\mu \boldsymbol{u}^\mu \, dV, \tag{2.15}$$

following De Souza Neto et al. (2015). Condition (2.14) can be rewritten as

$$\int_{\Omega^\mu} \boldsymbol{u}^F \, dV = \mathbf{0}, \tag{2.16}$$

using (2.11), and a microscale coordinate system located at the centroid of the unit cell[2]. This illustrates that the satisfaction of (2.14) leads to the elimination of rigid body translations from the kinematically admissible displacement fluctuations. Further, (2.15) is expressed as

$$\frac{1}{|\Omega^\mu|}\int_{\partial\Omega^\mu} \boldsymbol{u}^F \otimes \boldsymbol{n}^\mu \, dS = \mathbf{0}, \tag{2.17}$$

using (2.12) together with the divergence theorem. In the above, $\boldsymbol{n}^\mu$ is the outward unit normal on $\partial\Omega^\mu$. Therefore, the satisfaction of (2.15) leads to the elimination of rigid body rotations. The (2.16) and (2.17) conditions constitute the minimal set for kinematical admissibility of $\boldsymbol{u}^F$ in this multiscale framework (cf. De Souza Neto et al. (2015)).

The micro-to-macro transition is governed by the principle of multiscale virtual power, often referred to as the variational form of the Hill-Mandel condition (Hill (1972), Mandel (1971)), stated as

$$|\Omega^\mu| \delta\boldsymbol{F} : \boldsymbol{P} = \int_{\Omega^\mu} \delta\boldsymbol{F}^\mu : \boldsymbol{P}^\mu \, dV. \tag{2.18}$$

where $\boldsymbol{P}^\mu$ is the microscopic first Piola-Kirchhoff stress tensor. Equating $\delta\boldsymbol{u}^F = \mathbf{0}$ and utilizing the arbitrariness of $\delta\boldsymbol{F}$, reduces (2.18) to the stress homogenization relation

$$\boldsymbol{P} = \frac{1}{|\Omega^\mu|}\int_{\Omega^\mu} \boldsymbol{P}^\mu \, dV, \tag{2.19}$$

[2]Such a coordinate system satisfies $\int_{\Omega^\mu} \boldsymbol{X} \, dV = \mathbf{0}$, but any coordinate system located elsewhere could readily be translated to the center.

which can be rewritten[3] using the traction $\boldsymbol{t}^\mu = \boldsymbol{P}^\mu \cdot \boldsymbol{n}^\mu$ on $\partial\Omega^\mu$ and the divergence theorem, i.e.

$$\begin{aligned}
\boldsymbol{P} &= \frac{1}{|\Omega^\mu|}\int_{\Omega^\mu} \boldsymbol{P}^\mu \cdot \mathsf{1}\, dV = \frac{1}{|\Omega^\mu|}\int_{\Omega^\mu} \boldsymbol{P}^\mu \cdot \boldsymbol{\nabla}\boldsymbol{X}^\mu\, dV \\
&= \frac{1}{|\Omega^\mu|}\int_{\Omega^\mu} \left(\boldsymbol{\nabla}\cdot(\boldsymbol{P}^\mu \bar{\otimes} \boldsymbol{X}^\mu) - \boldsymbol{\nabla}\cdot\boldsymbol{P}^\mu \otimes \boldsymbol{X}^\mu\right) dV \\
&= \frac{1}{|\Omega^\mu|}\int_{\partial\Omega^\mu} (\boldsymbol{P}^\mu \bar{\otimes} \boldsymbol{X}^\mu)\cdot\boldsymbol{n}^\mu\, dS = \frac{1}{|\Omega^\mu|}\int_{\partial\Omega^\mu} (\boldsymbol{P}^\mu\cdot\boldsymbol{n}^\mu)\otimes\boldsymbol{X}^\mu\, dS \\
&= \frac{1}{|\Omega^\mu|}\int_{\partial\Omega^\mu} \boldsymbol{t}^\mu \otimes \boldsymbol{X}^\mu\, dS,
\end{aligned} \tag{2.20}$$

assuming microscopic equilibrium (2.13).

Previously, the *minimal* set of kinematical admissible displacement fluctuations was introduced, i.e. (2.16) and (2.17). As insinuated, the admissible set can be extended to include additional constraints. These constraints are readily identified by rewriting (2.18) using Hill's lemma (cf. Saeb et al. (2016))

$$\int_{\Omega^\mu} \delta\boldsymbol{F}^\mu : \boldsymbol{P}^\mu\, dV - |\Omega^\mu|\delta\boldsymbol{F} : \boldsymbol{P} = \int_{\partial\Omega^\mu} (\delta\boldsymbol{\varphi}^\mu - \delta\boldsymbol{F}\cdot\boldsymbol{X}^\mu)\cdot(\boldsymbol{t}^\mu - \boldsymbol{P}\cdot\boldsymbol{n}^\mu)\, dS = 0. \tag{2.21}$$

To prove that the equality (2.21) holds, the right hand side is expanded as

$$\begin{aligned}
&\int_{\partial\Omega^\mu} (\delta\boldsymbol{\varphi}^\mu - \delta\boldsymbol{F}\cdot\boldsymbol{X}^\mu)\cdot(\boldsymbol{t}^\mu - \boldsymbol{P}\cdot\boldsymbol{n}^\mu)\, dS \\
&= \int_{\partial\Omega^\mu} (\delta\boldsymbol{\varphi}^\mu - \delta\boldsymbol{F}\cdot\boldsymbol{X}^\mu)\cdot(\boldsymbol{P}^\mu\cdot\boldsymbol{n}^\mu - \boldsymbol{P}\cdot\boldsymbol{n}^\mu)\, dS \\
&= \int_{\partial\Omega^\mu} \delta\boldsymbol{\varphi}^\mu\cdot(\boldsymbol{P}^\mu\cdot\boldsymbol{n}^\mu)\, dS - \int_{\partial\Omega^\mu} \delta\boldsymbol{\varphi}^\mu\cdot(\boldsymbol{P}\cdot\boldsymbol{n}^\mu)\, dS \\
&- \int_{\partial\Omega^\mu} (\delta\boldsymbol{F}\cdot\boldsymbol{X}^\mu)\cdot\boldsymbol{P}^\mu\cdot\boldsymbol{n}^\mu\, dS + \int_{\partial\Omega^\mu} (\delta\boldsymbol{F}\cdot\boldsymbol{X}^\mu)\cdot\boldsymbol{P}\cdot\boldsymbol{n}^\mu\, dS \\
&= \int_{\partial\Omega^\mu} (\delta\boldsymbol{\varphi}^\mu\cdot\boldsymbol{P}^\mu)\cdot\boldsymbol{n}^\mu\, dS - \int_{\partial\Omega^\mu} \boldsymbol{P} : (\delta\boldsymbol{\varphi}^\mu\otimes\boldsymbol{n}^\mu)\, dS \\
&- \int_{\partial\Omega^\mu} \delta\boldsymbol{F} : ((\boldsymbol{P}^\mu\cdot\boldsymbol{n}^\mu)\otimes\boldsymbol{X}^\mu)\, dS + \int_{\partial\Omega^\mu} (\delta\boldsymbol{F}\cdot\boldsymbol{P}) : (\boldsymbol{X}^\mu\otimes\boldsymbol{n}^\mu)\, dS.
\end{aligned} \tag{2.22}$$

Via the divergence theorem and the extraction of macroscopic terms outside the integrals, (2.22) becomes

$$\begin{aligned}
&\int_{\Omega^\mu} \boldsymbol{\nabla}\cdot(\delta\boldsymbol{\varphi}^\mu\cdot\boldsymbol{P}^\mu)\, dV - \boldsymbol{P} : \int_{\partial\Omega^\mu} \delta\boldsymbol{\varphi}^\mu\otimes\boldsymbol{n}^\mu\, dS \\
&-\delta\boldsymbol{F} : \int_{\partial\Omega^\mu} (\boldsymbol{P}^\mu\cdot\boldsymbol{n}^\mu)\otimes\boldsymbol{X}^\mu\, dS + (\delta\boldsymbol{F}\cdot\boldsymbol{P}) : \int_{\partial\Omega^\mu} \boldsymbol{X}^\mu\otimes\boldsymbol{n}^\mu\, dS.
\end{aligned} \tag{2.23}$$

[3]The product $\bar{\otimes}$ between a second order tensor $\boldsymbol{B}$ and a vector $\boldsymbol{b}$ renders the third order tensor $\boldsymbol{A} = \boldsymbol{B}\bar{\otimes}\boldsymbol{b}$ with components $A_{jkl} = B_{jl}b_k$.

The first term of (2.23) is

$$\int_{\Omega^\mu} \boldsymbol{\nabla} \cdot (\delta\boldsymbol{\varphi}^\mu \cdot \boldsymbol{P}^\mu)\, dV = \int_{\Omega^\mu} (\delta\boldsymbol{F}^\mu : \boldsymbol{P}^\mu + \delta\boldsymbol{\varphi}^\mu \cdot (\boldsymbol{\nabla} \cdot \boldsymbol{P}^\mu))\, dV = \int_{\Omega^\mu} \delta\boldsymbol{F}^\mu : \boldsymbol{P}^\mu\, dV, \quad (2.24)$$

again assuming microscopic equilibrium (2.13). The second term of (2.23) is rewritten using the gradient theorem and the (2.15) homogenization relation, i.e.

$$\boldsymbol{P} : \int_{\partial\Omega^\mu} \delta\boldsymbol{\varphi}^\mu \otimes \boldsymbol{n}^\mu\, dS = \boldsymbol{P} : \int_{\Omega^\mu} \delta\boldsymbol{F}^\mu\, dV = |\Omega^\mu| \delta\boldsymbol{F} : \boldsymbol{P}, \quad (2.25)$$

whereas the third term of (2.23) becomes

$$\delta\boldsymbol{F} : \int_{\partial\Omega^\mu} (\boldsymbol{P}^\mu \cdot \boldsymbol{n}^\mu) \otimes \boldsymbol{X}^\mu\, dS = |\Omega^\mu| \delta\boldsymbol{F} : \boldsymbol{P}, \quad (2.26)$$

via the (2.20) relation. Lastly, the fourth term of (2.23) is

$$\begin{aligned} &(\delta\boldsymbol{F} \cdot \boldsymbol{P}) : \int_{\partial\Omega^\mu} \boldsymbol{X}^\mu \otimes \boldsymbol{n}^\mu\, dS = (\delta\boldsymbol{F} \cdot \boldsymbol{P}) : \int_{\Omega^\mu} \boldsymbol{\nabla} \boldsymbol{X}^\mu\, dV \\ &= (\delta\boldsymbol{F} \cdot \boldsymbol{P}) : \int_{\Omega^\mu} \mathbf{1}\, dV = |\Omega^\mu| \delta\boldsymbol{F} : \boldsymbol{P}. \end{aligned} \quad (2.27)$$

Combining (2.24) - (2.27) in (2.23) yields

$$\begin{aligned} &\int_{\Omega^\mu} \delta\boldsymbol{F}^\mu : \boldsymbol{P}^\mu\, dV - |\Omega^\mu| \delta\boldsymbol{F} : \boldsymbol{P} - |\Omega^\mu| \delta\boldsymbol{F} : \boldsymbol{P} + |\Omega^\mu| \delta\boldsymbol{F} : \boldsymbol{P} \\ &= \int_{\Omega^\mu} \delta\boldsymbol{F}^\mu : \boldsymbol{P}^\mu\, dV - |\Omega^\mu| \boldsymbol{P} : \delta\boldsymbol{F}, \end{aligned} \quad (2.28)$$

wherefore it has been shown that the equality in (2.21) holds. It is noted that (2.21) is satisfied for the following boundary conditions:

1) If $\boldsymbol{F}^\mu = \boldsymbol{F} = \boldsymbol{B}$ in Ω^μ for any constant second order tensor $\boldsymbol{B}$, then $\boldsymbol{u}^F = \mathbf{0}$ and $\boldsymbol{\varphi}^\mu = \boldsymbol{B} \cdot \boldsymbol{X}^\mu$ must hold in Ω^μ according to (2.11). Accordingly, $\delta\boldsymbol{F}^\mu = \delta\boldsymbol{F} = \mathbf{0}$ in Ω^μ and the left hand side of (2.21) vanishes, i.e.

$$\int_{\Omega^\mu} (\delta\boldsymbol{F}^\mu : \boldsymbol{P}^\mu - \delta\boldsymbol{F} : \boldsymbol{P})\, dV = 0. \quad (2.29)$$

This condition corresponds to *constant deformation* in Ω^μ, and is usually referred to as Taylor's (or in the linear elastic regime, Voigt's) assumption (Taylor (1938)).

2) If $\boldsymbol{\varphi}^\mu = \boldsymbol{F} \cdot \boldsymbol{X}^\mu$ on $\partial\Omega^\mu$, then $\boldsymbol{u}^F = \mathbf{0}$ must hold on $\partial\Omega^\mu$ according to (2.11). Also, $\delta\boldsymbol{\varphi}^\mu = \delta\boldsymbol{F} \cdot \boldsymbol{X}^\mu$ such that the right hand side of (2.21) vanishes, i.e.

$$\int_{\partial\Omega^\mu} (\delta\boldsymbol{\varphi}^\mu - \delta\boldsymbol{F} \cdot \boldsymbol{X}^\mu) \cdot (\boldsymbol{t}^\mu - \boldsymbol{P} \cdot \boldsymbol{n}^\mu)\, dS = 0. \quad (2.30)$$

This condition yields *linear boundary displacements* on $\partial\Omega^\mu$.

3) If instead $(\boldsymbol{\varphi}^\mu - \delta\boldsymbol{F}\cdot\boldsymbol{X}^\mu)$ is periodic and $(\boldsymbol{t}^\mu - \boldsymbol{P}\cdot\boldsymbol{n}^\mu)$ is anti-periodic with respect to the translation $\boldsymbol{A}$ on $\partial\Omega^\mu$, the right hand side of (2.21) vanishes, i.e.

$$
\begin{aligned}
&\int_{\partial\Omega^\mu} (\delta\boldsymbol{\varphi}^\mu(\boldsymbol{X}^\mu) - \delta\boldsymbol{F}\cdot\boldsymbol{X}^\mu)\cdot(\boldsymbol{t}^\mu(\boldsymbol{X}^\mu) - \boldsymbol{P}\cdot\boldsymbol{n}^\mu(\boldsymbol{X}^\mu))\; dS \\
&= \int_{\partial\Omega^{\mu+}} (\delta\boldsymbol{\varphi}^\mu(\boldsymbol{X}^\mu) - \delta\boldsymbol{F}\cdot\boldsymbol{X}^\mu)\cdot(\boldsymbol{t}^\mu(\boldsymbol{X}^\mu) - \boldsymbol{P}\cdot\boldsymbol{n}^\mu(\boldsymbol{X}^\mu))\; dS \\
&+ \int_{\partial\Omega^{\mu-}} (\delta\boldsymbol{\varphi}^\mu(\boldsymbol{X}^\mu) - \delta\boldsymbol{F}\cdot\boldsymbol{X}^\mu(\boldsymbol{X}^\mu))\cdot(\boldsymbol{t}^\mu(\boldsymbol{X}^\mu) - \boldsymbol{P}\cdot\boldsymbol{n}^\mu(\boldsymbol{X}^\mu))\; dS \\
&= \int_{\partial\Omega^{\mu+}} (\delta\boldsymbol{\varphi}^\mu(\boldsymbol{X}^\mu) - \delta\boldsymbol{F}\cdot\boldsymbol{X}^\mu)\cdot(\boldsymbol{t}^\mu(\boldsymbol{X}^\mu) - \boldsymbol{P}\cdot\boldsymbol{n}^\mu(\boldsymbol{X}^\mu))\; dS \\
&+ \int_{\partial\Omega^{\mu+}} (\delta\boldsymbol{\varphi}^\mu(\boldsymbol{X}^\mu - \boldsymbol{A}) - \delta\boldsymbol{F}\cdot(\boldsymbol{X}^\mu - \boldsymbol{A}))\cdot(\boldsymbol{t}^\mu(\boldsymbol{X}^\mu - \boldsymbol{A}) - \boldsymbol{P}\cdot\boldsymbol{n}^\mu(\boldsymbol{X}^\mu - \boldsymbol{A}))\; dS \\
&= \int_{\partial\Omega^{\mu+}} (\delta\boldsymbol{\varphi}^\mu(\boldsymbol{X}^\mu) - \delta\boldsymbol{F}\cdot\boldsymbol{X}^\mu)\cdot(\boldsymbol{t}^\mu(\boldsymbol{X}^\mu) - \boldsymbol{P}\cdot\boldsymbol{n}^\mu(\boldsymbol{X}^\mu))\; dS \\
&- \int_{\partial\Omega^{\mu+}} (\delta\boldsymbol{\varphi}^\mu(\boldsymbol{X}^\mu) - \delta\boldsymbol{F}\cdot\boldsymbol{X}^\mu)\cdot(\boldsymbol{t}^\mu(\boldsymbol{X}^\mu) - \boldsymbol{P}\cdot\boldsymbol{n}^\mu(\boldsymbol{X}^\mu))\; dS = 0.
\end{aligned}
\tag{2.31}
$$

The periodicity of $(\boldsymbol{\varphi}^\mu - \delta\boldsymbol{F}\cdot\boldsymbol{X}^\mu)$ and anti-periodicity of $(\boldsymbol{t}^\mu - \boldsymbol{P}\cdot\boldsymbol{n}^\mu)$ ultimately requires

$$
\left.
\begin{aligned}
\boldsymbol{u}^F(\boldsymbol{X}^\mu) &= \boldsymbol{u}^F(\boldsymbol{X}^\mu - \boldsymbol{A}) \\
\boldsymbol{t}^\mu(\boldsymbol{X}^\mu) &= -\boldsymbol{t}^\mu(\boldsymbol{X}^\mu - \boldsymbol{A})
\end{aligned}
\right\} \text{ for } \boldsymbol{X}^\mu \in \partial\Omega^{\mu+}, \tag{2.32}
$$

where the inherent anti-periodicity of the normal vector $\boldsymbol{n}^\mu$ on $\partial\Omega^\mu$ was used. The (2.32) conditions are referred to as *periodic boundary conditions* on $\partial\Omega^\mu$.

4) If $\boldsymbol{t}^\mu = \boldsymbol{P}\cdot\boldsymbol{n}^\mu = \boldsymbol{P}^\mu\cdot\boldsymbol{n}^\mu = \boldsymbol{c}$ on $\partial\Omega^\mu$ for any constant vector $\boldsymbol{c}$, the right hand side of (2.21) vanishes. This condition results in *constant boundary tractions* on $\partial\Omega^\mu$.

5) If $\boldsymbol{P}^\mu = \boldsymbol{P} = \boldsymbol{B}$ in Ω^μ the left hand side of (2.21) vanishes due to the (2.17) condition, i.e.

$$
\boldsymbol{B} : \int_{\Omega^\mu} (\delta\boldsymbol{F}^\mu - \delta\boldsymbol{F})\; dV = \boldsymbol{B} : \int_{\Omega^\mu} \boldsymbol{\nabla}^\mu\delta\boldsymbol{u}^F\; dV = \boldsymbol{B} : \int_{\partial\Omega^\mu} \delta\boldsymbol{u}^F \otimes \boldsymbol{n}^\mu\; dS = 0. \tag{2.33}
$$

This condition yields *constant stress* in Ω^μ, and is usually referred to as Sachs' (or in the linear elastic regime, Reuss') assumption (Sachs (1928)).

It can be shown that 4) is equivalent to the minimal set of admissible displacement fluctuations, cf. De Souza Neto et al. (2015) and Zhang et al. (2021). Taylor assumes uniform deformation in Ω^μ, which violates the stress equilibrium of multiphase composites. On the other hand, Sachs assumes uniform stress in Ω^μ, which violates the displacement compatibility. Although Taylor's and Sachs' assumptions provide very rough estimates of the actual behavior of a multiphase composites, they

yield upper (stiff) and lower (compliant) bounds on the elastic strain energy, respectively. For purely mechanical problems, the effective behavior derived under the 3) periodic boundary conditions is bounded from above by the 2) linear displacement boundary conditions, and from below by the 4) constant traction boundary condition, cf. Saeb et al. (2016).

2.2.1 Periodic boundary conditions

Although the results obtained under periodic boundary conditions must not be closest to the exact solution, they are often employed in practice when assuming a periodic microstructure, as is done herein. The periodic kinematic constraints[4] on $\boldsymbol{u}^F$ are

$$\boldsymbol{u}^F(\boldsymbol{X}^\mu) = \boldsymbol{u}^F(\boldsymbol{X}^\mu - \boldsymbol{A}_j) \quad \text{at} \quad \boldsymbol{X}^\mu \in \partial\Omega^{\mu j+}, \quad j = 1, 2, \tag{2.34}$$

or, using (2.11), equivalently cast on $\boldsymbol{u}^\mu$

$$\boldsymbol{u}^\mu(\boldsymbol{X}^\mu) - \boldsymbol{u}^\mu(\boldsymbol{X}^\mu - \boldsymbol{A}_j) = (\boldsymbol{F} - \boldsymbol{1}) \cdot \boldsymbol{A}_j \quad \text{at} \quad \boldsymbol{X}^\mu \in \partial\Omega^{\mu j+}, \quad j = 1, 2. \tag{2.35}$$

To enforce the (2.35) constraints, a weak approach is employed, wherein the Hill-Mandel condition (2.18) is augmented using the Lagrange multipliers $\boldsymbol{\Lambda}^\mu = \boldsymbol{\Lambda}^\mu(\boldsymbol{X}^\mu)$

$$\begin{aligned} &|\Omega^\mu| \delta\boldsymbol{F}(\boldsymbol{X}) : \boldsymbol{P}(\boldsymbol{X}) - \int_{\Omega^\mu} \delta\boldsymbol{F}^\mu(\boldsymbol{X}^\mu) : \boldsymbol{P}^\mu(\boldsymbol{X}^\mu)\, dV \\ &+ \sum_{j=1}^{2} \int_{\partial\Omega^{\mu j+}} \boldsymbol{\Lambda}^\mu(\boldsymbol{X}^\mu) \cdot (\delta\boldsymbol{u}^\mu(\boldsymbol{X}^\mu) - \delta\boldsymbol{u}^\mu(\boldsymbol{X}^\mu - \boldsymbol{A}_j) - \delta\boldsymbol{F}(\boldsymbol{X}) \cdot \boldsymbol{A}_j)\, dS \\ &+ \sum_{j=1}^{2} \int_{\partial\Omega^{\mu j+}} \delta\boldsymbol{\Lambda}^\mu(\boldsymbol{X}^\mu) \cdot (\boldsymbol{u}^\mu(\boldsymbol{X}^\mu) - \boldsymbol{u}^\mu(\boldsymbol{X}^\mu - \boldsymbol{A}_j) - (\boldsymbol{F}(\boldsymbol{X}) - \boldsymbol{1}) \cdot \boldsymbol{A}_j)\, dS = 0. \end{aligned} \tag{2.36}$$

Equation (2.36) holds for any $\delta\boldsymbol{\Lambda}^\mu$, $\delta\boldsymbol{F}$ and $\delta\boldsymbol{u}^\mu \in \mathcal{U}$, where $\mathcal{U} = \{\boldsymbol{u}^\mu \in H^1 : \boldsymbol{u}^\mu(\boldsymbol{X}_u^\mu) = \boldsymbol{0}\}$ enforces (2.16) through the restriction of motion of a single material point $\boldsymbol{X}_u^\mu \in \Omega_u^\mu$.

To glean more insight into (2.36), is it assumed that $\delta\boldsymbol{F} = \boldsymbol{0}$ and $\delta\boldsymbol{\Lambda}^\mu = \boldsymbol{0}$, such that (2.18) becomes

$$\int_{\Omega^\mu} \delta\boldsymbol{F}^\mu(\boldsymbol{X}^\mu) : \boldsymbol{P}^\mu(\boldsymbol{X}^\mu)\, dV - \sum_{j=1}^{2} \int_{\partial\Omega_j^+} \boldsymbol{\Lambda}^\mu \cdot (\delta\boldsymbol{u}^\mu(\boldsymbol{X}^\mu) - \delta\boldsymbol{u}^\mu(\boldsymbol{X}^\mu - \boldsymbol{A}_j))\, dS = 0, \tag{2.37}$$

or, using the product rule in combination with the divergence theorem

$$\begin{aligned} &\int_\Omega (\boldsymbol{\nabla}^\mu \cdot \boldsymbol{P}^\mu(\boldsymbol{X}^\mu)) \cdot \delta\boldsymbol{u}^\mu(\boldsymbol{X}^\mu)\, dV \\ &- \sum_{j=1}^{2} \int_{\partial\Omega^{\mu j+}} (\boldsymbol{P}^\mu(\boldsymbol{X}^\mu) \cdot \boldsymbol{n}^\mu(\boldsymbol{X}^\mu) + \boldsymbol{\Lambda}^\mu(\boldsymbol{X}^\mu)) \cdot \delta\boldsymbol{u}^\mu(\boldsymbol{X}^\mu)\, dS \\ &- \sum_{j=1}^{2} \int_{\partial\Omega^{\mu j-}} (\boldsymbol{P}^\mu(\boldsymbol{X}^\mu) \cdot \boldsymbol{n}^\mu(\boldsymbol{X}^\mu) - \boldsymbol{\Lambda}^\mu(\boldsymbol{X}^\mu + \boldsymbol{A}_j)) \cdot \delta\boldsymbol{u}^\mu(\boldsymbol{X}^\mu)\, dS = 0. \end{aligned} \tag{2.38}$$

[4]The assumption of rectangular unit cells hold.

From (2.38), the quasi-static local microscopic equilibrium equations are found, i.e.

$$\begin{aligned}
&\boldsymbol{\nabla}^{\mu} \cdot \boldsymbol{P}^{\mu}(\boldsymbol{X}^{\mu}) = \mathbf{0} \ \text{ in } \ \Omega^{\mu}, \\
&\boldsymbol{P}^{\mu}(\boldsymbol{X}^{\mu})\boldsymbol{n}^{\mu}(\boldsymbol{X}^{\mu}) = -\boldsymbol{\Lambda}^{\mu}(\boldsymbol{X}^{\mu}) \ \text{ at } \ \boldsymbol{X}^{\mu} \in \partial\Omega^{\mu j+}, \\
&\boldsymbol{P}^{\mu}(\boldsymbol{X}^{\mu})\boldsymbol{n}^{\mu}(\boldsymbol{X}^{\mu}) = \boldsymbol{\Lambda}^{\mu}(\boldsymbol{X}^{\mu} + \boldsymbol{A}_j) \ \text{ at } \ \boldsymbol{X}^{\mu} \in \partial\Omega^{\mu j-},
\end{aligned} \tag{2.39}$$

using the arbitrariness of $\delta\boldsymbol{u}^{\mu}$. Here, the physical interpretation of the Lagrange multipliers, $\boldsymbol{\Lambda}^{\mu}$, becomes apparent, i.e. they act as anti-periodic boundary tractions which enforce the periodicity constraints (2.35). Hereby, it has been verified that the (2.32) periodic boundary constraints are fulfilled.

2.2.2 Homogenized stress and tangent tensors

The stress homogenization relation appears in (2.19). However, by equating $\delta\boldsymbol{F} = \mathbf{0}$, $\delta\boldsymbol{\Lambda}^{\mu} = \mathbf{0}$ and $\delta\boldsymbol{u}^{F} = \boldsymbol{B} \cdot \boldsymbol{X}^{\mu}$ in (2.36), it is found that

$$\int_{\Omega^{\mu}} \boldsymbol{P}^{\mu}(\boldsymbol{X}^{\mu}) dV = \sum_{j=1}^{2} \int_{\partial\Omega^{\mu j+}} \boldsymbol{\Lambda}^{\mu}(\boldsymbol{X}^{\mu}) \otimes \boldsymbol{A}_j \, dS, \tag{2.40}$$

must hold for arbitrary $\boldsymbol{B}$. By inserting (2.40) in (2.19), it appears that the homogenized stress also can be computed from $\boldsymbol{\Lambda}^{\mu}$, i.e.

$$\boldsymbol{P}(\boldsymbol{X}) = \frac{1}{|\Omega^{\mu}|} \sum_{j=1}^{2} \int_{\partial\Omega^{\mu j+}} \boldsymbol{\Lambda}^{\mu}(\boldsymbol{X}^{\mu}) \otimes \boldsymbol{A}_j \, dS. \tag{2.41}$$

Lastly, it is noted that the homogenized fourth order incremental elasticity tensor is obtained as

$$\boldsymbol{L}(\boldsymbol{X}) = \frac{\partial \boldsymbol{P}}{\partial \boldsymbol{F}}. \tag{2.42}$$

Herein, the inverse homogenization, i.e. optimization of the material distribution in the unit cell, is restricted to the evaluation of the homogenized stress, wherefore additional details regarding the homogenization of the tangent stiffness tensor are omitted. More details appear in e.g. Saeb et al. (2016) and Zhang et al. (2021).

2.2.3 FE formulation

A total Lagrangian, Galerkin FE formulation equivalent to the approach described in Sec. 2.1.2 is employed to solve (2.36). However, unlike the quasi-static case of (2.3) where $\boldsymbol{u}^{\mu}$ is the single unknown field, the solution to (2.36) involves the additional fields $\boldsymbol{F}$ and $\boldsymbol{\Lambda}^{\mu}$. The first, $\boldsymbol{F}$, is hereafter posed as $\mathsf{F} = [F_{11},\, F_{21},\, F_{12},\, F_{22}]^T$ in two-dimensions. In the Papers C and D, structured finite element meshes are used to discretize the unit cells, which facilitates the application of the periodicity constraints, since they are applied nodal-wise. It is assumed that there exist m pairs of mating boundary nodes on $\partial\Omega$.

This FE-discretization results in that (2.36) becomes

$$\delta \mathsf{u}^{\mu,T} \left(\mathsf{T}^T \boldsymbol{\Lambda}^\mu - \sum\!\!\!\!\!\!\int_{\Omega^e} \boldsymbol{\nabla} \mathsf{N}^T \mathsf{P}^\mu \, dV \right) + \delta \mathsf{F}^T \left(|\Omega| \mathsf{P} - \mathsf{H}^T \boldsymbol{\Lambda}^\mu \right) + \delta \boldsymbol{\Lambda}^{\mu,T} \left(\mathsf{T} \mathsf{u}^\mu - \mathsf{H} \boldsymbol{\nabla} \mathsf{u} \right) = 0, \tag{2.43}$$

where $\mathsf{H} \in \mathbb{R}^{2m \times 4}$ is introduced such that $\mathsf{H} \boldsymbol{\nabla} \mathsf{u} = (\boldsymbol{F} - \mathsf{1}) \cdot \boldsymbol{A}_j$, and $\mathsf{T} \in \mathbb{R}^{2m \times n}$ is the transformation matrix $\mathsf{u}^{\mu+} - \mathsf{u}^{\mu-} = \mathsf{T} \mathsf{u}^\mu$, where $\mathsf{u}^{\mu\pm} \in \mathbb{R}^{2m}$ denotes nodal microscopic displacement field values on $\partial \Omega^{\mu\pm}$ (cf. Zhang and Khandelwal (2020)). In this way, H is constructed as

$$\mathsf{H} = \left[\mathsf{H}_{11}, \, \mathsf{H}_{21}, \, \mathsf{H}_{12}, \, \mathsf{H}_{22} \right] = \begin{bmatrix} \Delta X_1^\mu & 0 & \Delta Y_1^\mu & 0 \\ 0 & \Delta X_1^\mu & 0 & \Delta Y_1^\mu \\ \Delta X_2^\mu & 0 & \Delta Y_2^\mu & 0 \\ 0 & \Delta X_2^\mu & 0 & \Delta Y_2^\mu \\ \vdots & \vdots & \vdots & \vdots \\ \Delta X_m^\mu & 0 & \Delta Y_m^\mu & 0 \\ 0 & \Delta X_m^\mu & 0 & \Delta Y_m^\mu \end{bmatrix}, \tag{2.44}$$

where e.g. $\Delta X_1^\mu = X_1^{\mu+} - X_1^{\mu-}$. The macroscopic loading conditions on the unit cell are enforced via the prescription of the macroscopic deformation gradient, i.e. any component of $\boldsymbol{\nabla} \mathsf{u}$, wherefore the corresponding component of $\delta \mathsf{F}$ vanishes, or the macroscopic stress, i.e. any component of P, cf. (2.43). If it is assumed that the macroscopic response it at least orthotropic, $\nabla u_{12} = 0$ and $\nabla u_{21} = 0$ for any biaxial stress state, cf. Wallin and Tortorelli (2020). For example, to mimic uniaxial loading conditions, a uniaxial $\nabla u_{11} \neq 0$ is prescribed together with the transversal stress condition $P_{22} = 0$[5]. Using the arbitrariness of $\delta \mathsf{u}$, $\delta \boldsymbol{\Lambda}^\mu$ and $\delta \mathsf{F}$ in (2.43), the residual equations

$$\mathsf{r}^*(\mathsf{u}^*) = \begin{bmatrix} \mathsf{r}_{\mathsf{u}^\mu} \\ \mathsf{r}_{\boldsymbol{\Lambda}^\mu} \\ \mathsf{r}_{\boldsymbol{F}} \end{bmatrix} = \mathsf{0}, \tag{2.45}$$

are found, where $\mathsf{r}_{\mathsf{u}^\mu} = \sum\!\!\!\!\!\!\int_{\Omega^e} \boldsymbol{\nabla} \mathsf{N}^T \mathsf{P}^\mu \, dV - \mathsf{T}^T \boldsymbol{\Lambda}^\mu$, $\mathsf{r}_{\boldsymbol{\Lambda}^\mu} = -\mathsf{T} \mathsf{u}^\mu + \mathsf{H} \boldsymbol{\nabla} \mathsf{u}$ and $\mathsf{r}_{\boldsymbol{F}} = -|\Omega| \mathsf{P} + \mathsf{H}^T \boldsymbol{\Lambda}^\mu$. The non-linear system of equations (2.45) can be solved using iterative methods such as the Newton-Raphson method (cf. Sec. 2.1.2) or path-following methods (cf. Crisfield (1993) and Leon et al. (2014)).

[5]Note that $P_{22} = 0$ is required, i.e. the first Piola-Kirchhoff stress is used rather than the Cauchy stress $\boldsymbol{\sigma}$. However, since $F_{12} = F_{21} = 0$ the $P_{22} = 0$ condition is equivalent to $\sigma_{22} = 0$.

3 Eigenvalue problems in structural analyzes

This section describes three eigenvalue problems that typically arise in structural analyzes. The first is encountered in the *free vibration* analysis of a structure, wherein the frequent aim is to survey the eigenfrequencies such that resonance is avoided at operating conditions. Another eigenvalue problem appears in *structural stability* analyzes, since the eigenvalues of the Hessian of the potential energy dictates its definiteness, i.e. stability properties of the system. Here, instabilities can be wanted or unwanted, depending on the application. The last eigenvalue problem is similar to that of the structural free vibration analysis, except that it is posed at the microscopic level, i.e. instead considers *elastic wave propagation* in a periodic media. By solving numerous eigenvalues problems for different propagation directions, a band-diagram is constructed which describes the dispersive properties of the material. The aforementioned eigenvalue problems are involved in Papers A, B and C, respectively.

3.1 Free vibration

The conventional free vibration analysis of a structure is conducted for vanishing initial strain, i.e. in the undeformed configuration. However, it is not uncommon for a mechanical structure to be assembled under non-vanishing strains, and certainly common for an assembled structure to be exposed to finite deformations, which in both cases ordinarily affects its static and dynamic behavior. In Paper A, the pre-strain's effect on the dynamical behavior of structures is investigated.

The computations are based on the small on large deformation framework (Ogden (2007)), wherein an time-dependent incremental deformation, $\mathring{\boldsymbol{u}}(\boldsymbol{X}, t)$, is superimposed on a pre-strained configuration in quasi-static equilibrium, defined by the displacement $\boldsymbol{u}_c(\boldsymbol{X})$. For any material point $\boldsymbol{X} \in \Omega$, the equations of motion at time t is (cf. (2.2))

$$\boldsymbol{\nabla} \cdot \boldsymbol{P}(\boldsymbol{\nabla u}) = \rho \frac{\partial^2 \boldsymbol{u}}{\partial t^2}, \tag{3.1}$$

using a slight abuse of notation[6]. The split

$$\boldsymbol{u}(\boldsymbol{X}, t) = \boldsymbol{u}_c(\boldsymbol{X}) + \mathring{\boldsymbol{u}}(\boldsymbol{X}, t), \tag{3.2}$$

results in that (3.1) becomes

$$\boldsymbol{\nabla} \cdot \boldsymbol{P}(\boldsymbol{\nabla u}_c + \boldsymbol{\nabla} \mathring{\boldsymbol{u}}) = \rho \frac{\partial^2 \mathring{\boldsymbol{u}}}{\partial t^2}. \tag{3.3}$$

A Taylor series expansion of the left hand side of (3.3) at $\boldsymbol{u}_c$ while ignoring higher order terms yields

$$\boldsymbol{\nabla} \cdot \boldsymbol{P}(\boldsymbol{\nabla u}_c + \boldsymbol{\nabla} \mathring{\boldsymbol{u}}) \approx \boldsymbol{\nabla} \cdot \boldsymbol{P}(\boldsymbol{\nabla u}_c) + \boldsymbol{\nabla} \cdot \left[\boldsymbol{L}(\boldsymbol{\nabla u}_c) : \boldsymbol{\nabla} \mathring{\boldsymbol{u}} \right]. \tag{3.4}$$

Since the body is assumed to be in quast-static equilibrium at $\boldsymbol{u}_c$, it holds that $\boldsymbol{\nabla} \cdot \boldsymbol{P}(\boldsymbol{\nabla u}_c) = \boldsymbol{0}$, why (3.4) inserted in (3.3) becomes

$$\boldsymbol{\nabla} \cdot \left[\boldsymbol{L}(\boldsymbol{\nabla u}_c) : \boldsymbol{\nabla} \mathring{\boldsymbol{u}} \right] = \rho \frac{\partial^2 \mathring{\boldsymbol{u}}}{\partial t^2}. \tag{3.5}$$

[6]For example, $\boldsymbol{u} = \boldsymbol{u}(\boldsymbol{X}, t)$.

Of course, (3.5) depicts a *linearized* relation, i.e. $\boldsymbol{L}$ does not depend on $\boldsymbol{\nabla}\mathring{\boldsymbol{u}}$. Now, using separation of variables, the solutions to (3.5) are posed as the harmonic oscillations

$$\mathring{\boldsymbol{u}}(\boldsymbol{X},t) = \boldsymbol{\phi}(\boldsymbol{X})e^{-i\omega t}, \tag{3.6}$$

where $\boldsymbol{\phi} : \Omega \to \mathbb{R}^2$ is the mode shape, $i = \sqrt{-1}$ and $\omega \in \mathbb{R}$ is the angular frequency[7]. Inserting (3.6) in (3.5), and noting that $e^{-i\omega t}$ is spatially independent and non-vanishing, results in the (local) eigenvalue problem

$$\frac{1}{\rho}\boldsymbol{\nabla}\cdot[\boldsymbol{L} : \boldsymbol{\nabla}\boldsymbol{\phi}] = -\omega^2\boldsymbol{\phi} \text{ in } \Omega, \tag{3.7}$$

with eigenpairs $(-\omega^2, \boldsymbol{\phi})$.

The eigenvalue problem (3.7), can be posed over the body Ω, by finding those $\boldsymbol{\phi} \in \{\boldsymbol{\phi} \in H^1 : \boldsymbol{\phi}(\boldsymbol{X}) = \boldsymbol{0} \text{ for } \boldsymbol{X} \in \partial\Omega_u\}$ which satisfy the weak form

$$\int_\Omega \boldsymbol{\nabla}\delta\boldsymbol{\phi}\cdot[\boldsymbol{L} : \boldsymbol{\nabla}\boldsymbol{\phi}]\, dV = \int_\Omega \rho\omega^2\delta\boldsymbol{\phi}\cdot\boldsymbol{\phi}\, dV, \tag{3.8}$$

for all smooth admissible $\delta\boldsymbol{\phi}$[8]. Using the arbitrariness of $\delta\boldsymbol{\phi}$, the discretization of (3.7) using the FE-method (FEM) described in Sect. 2.1.2, yields the generalized eigenvalue problem

$$\mathsf{K}\boldsymbol{\phi}_j = \omega_j^2\mathsf{M}\boldsymbol{\phi}_j, \quad j \in \mathbb{N}_n, \tag{3.9}$$

where it is emphasized that the stiffness matrix $\mathsf{K} = \mathsf{K}(\mathsf{u}_c)$, i.e. the eigenpairs $(\omega_j^2, \boldsymbol{\phi}_j)$ depend on the quasi-static equilibrium displacements u_c. Due to the hyperelastic assumption, K is symmetric and real, as is the mass matrix M. The eigenvalues are assumed to be sorted in ascending order, and their associated eigenmodes are mass-orthogonalized.

3.2 Structural stability

An equilibrium position of a conservative system is stable if the potential energy in that position has a (local) isolated minimum. This condition is equivalent to the requirement that the second variation of the potential energy is positive definite, i.e. all eigenvalues of the tangent stiffness matrix, K in (2.10), are strictly positive. In contrast, an unstable equilibrium position is characterized by an indefinite K, i.e. which has at least one eigenvalue which is strictly less than zero. A system that transitions from being stable to unstable must pass a *singular point*, in which at least one eigenvalue of K vanishes. To summarize, it holds that

$$\boldsymbol{\phi}^T\mathsf{K}\boldsymbol{\phi} \begin{cases} > 0 \text{ for all } \boldsymbol{\phi} \in \mathbb{R}^n \setminus \{\boldsymbol{0}\} \text{ (Stable)}, \\ = 0 \text{ for at least one } \boldsymbol{\phi} \in \mathbb{R}^n \setminus \{\boldsymbol{0}\} \text{ (Singular)}, \\ < 0 \text{ for at least one } \boldsymbol{\phi} \in \mathbb{R}^n \setminus \{\boldsymbol{0}\} \text{ (Unstable)}. \end{cases} \tag{3.10}$$

[7]Due to the hyperelastic assumption, $\boldsymbol{L}$ is real and possesses major symmetry, wherefore the angular frequencies (eigenvalues) are real.

[8]Here, free vibrations are assumed, in combination with the assumption that $\delta\boldsymbol{\phi}$ vanishes where the Dirichlet constraints are imposed on $\boldsymbol{u}$.

Typically, the probe of singular points is of uttermost importance, irrelevant of whether the unstable structural behavior is wanted or not. Therefore, it is emphasized that in a singular, or so-called *critical*, point it hold that

$$\mathbf{K}\boldsymbol{\phi}_j = \mathbf{0}, \quad j \in \mathbb{N}_n, \tag{3.11}$$

has a nontrivial solution $\boldsymbol{\phi}_j$.

Let us examine the neighborhood of an equilibrium critical point $(\mathbf{u}^c, \lambda^c)$, where $\lambda \in \mathbb{R}$ denotes the external load magnitude, i.e. $\mathbf{F}_{ext} = \lambda \mathbf{l}$, cf. (2.8). To this end, $\mathbf{u}$ and λ are parameterized such that $\mathbf{u} = \mathbf{u}(s)$ and $\lambda = \lambda(s)$, where s is the parameter which describes the equilibrium path in the vicinity of the critical point, such that $(\mathbf{u}(0), \lambda(0)) = (\mathbf{u}^c, \lambda^c)$. A truncated Taylor series expansion of the quasi-static residual (2.8) with respect to s at $s = 0$ yields

$$\mathbf{r}(\mathbf{u}(s), \lambda(s)) \approx \mathbf{r}(\mathbf{u}^c, \lambda^c) + \frac{\partial \mathbf{r}(\mathbf{u}^c, \lambda^c)}{\partial \mathbf{u}} \frac{\partial \mathbf{u}}{\partial s} s + \frac{\partial \mathbf{r}(\mathbf{u}^c, \lambda^c)}{\partial \lambda} \frac{\partial \lambda}{\partial s} s = \mathbf{0}. \tag{3.12}$$

Using (2.8), (2.10) and $s \neq 0$ in (3.12) results in

$$\mathbf{K}(\mathbf{u}^c, \lambda^c) \frac{\partial \mathbf{u}}{\partial s} - \mathbf{l} \frac{\partial \lambda}{\partial s} = \mathbf{0}, \tag{3.13}$$

By premultiplying (3.13) by an eigenvector $\boldsymbol{\phi}_j$ to $\mathbf{K}(\mathbf{u}^c, \lambda^c)$, it is found that

$$\boldsymbol{\phi}_j^T \mathbf{l} \frac{\partial \lambda}{\partial s} = \mathbf{0}, \tag{3.14}$$

since $\boldsymbol{\phi}_j^T \mathbf{K}(\mathbf{u}^c, \lambda^c) \frac{\partial \mathbf{u}}{\partial s} = \mathbf{0}$, cf. (3.11). Equation (3.14) reveals three possibilities, either 1) $\boldsymbol{\phi}_j^T \mathbf{l} \neq \mathbf{0}$ and $\frac{\partial \lambda}{\partial s} = 0$, 2) $\boldsymbol{\phi}_j^T \mathbf{l} = \mathbf{0}$ and $\frac{\partial \lambda}{\partial s} \neq 0$ or 3) $\boldsymbol{\phi}_j^T \mathbf{l} = \mathbf{0}$ and $\frac{\partial \lambda}{\partial s} = 0$. Case 1) corresponds to a *limit point* in which the system cannot sustain a positive increment in the load magnitude, 2) is a *bifurcation point*, in which multiple equilibrium paths cross, i.e. no unique solution exists, and 3) is a combination of both of the aforementioned events.

3.2.1 Identification of critical points

There exist two commonly used methods for identifying the critical point. The first, known as the extended system approach, directly computes the critical configurations by restricting the set of solutions to those which are singular (Wriggers (2008)). To this end, the (3.11) condition is appended as constraint to the weak form, which results in the new set of discretized residual equations

$$\begin{bmatrix} \mathbf{r} \\ \mathbf{K}\boldsymbol{\phi} \\ \|\boldsymbol{\phi}\|_2 - 1 \end{bmatrix} = \mathbf{0}, \tag{3.15}$$

where the last condition excludes trivial solutions to (3.11). The (3.15) extended system is limited to the computation of *simple* critical points, i.e. the eigenvector corresponding to a single zero-eigenvalue of $\mathbf{K}$. The nonlinear system of equations (3.15) is solved using a traditional Newton-Raphson iterative

scheme, wherein partitioning is used to reduce the computational effort, cf. Wriggers (2008). The extended system approach provides an exact measure of the critical loads up to a numerical tolerance.

The second approach, known as the one point approach, approximates the critical load levels by extrapolating information provided at a stable equilibrium configuration. Instead of solving (3.11) explicitly, a decomposition of the tangent stiffness matrix is introduced, which turns (3.11) into a generalized eigenvalue problem. This approach is inspired by the so-called *linearized buckling* approach, in which the initial displacements are assumed to be small, wherefore the u which solves the linear system

$$\mathsf{K}_L \mathsf{u} = \mathsf{F}_{ext}, \tag{3.16}$$

is accepted as reference solution, where $\mathsf{K}_L = \mathsf{K}(\mathsf{0})$ is the linear stiffness matrix. Due to the linearity of (3.16), any change in load $\mathsf{F}_{ext} \rightarrow \lambda \mathsf{F}_{ext}$ result in an equal change in displacement $\mathsf{u} \rightarrow \lambda \mathsf{u}$, and equivalently for the linear stresses $\boldsymbol{\sigma}^L \rightarrow \lambda \boldsymbol{\sigma}^L$. It is further assumed that the change in stress affects the stiffness matrix, such that $\mathsf{K}_L \rightarrow \mathsf{K}_L + \lambda \mathsf{K}_G$, where K_G is the so-called geometric stiffness matrix which depends explicitly on the stresses $\boldsymbol{\sigma}^L$. Therefore, an approximation of the critical load $\mathsf{F}^c_{ext} = \lambda_c \mathsf{F}_{ext}$ is given by the $\lambda_c = \min_{j \in \mathbb{N}_n} \lambda_j$ which fulfill

$$(\mathsf{K}_L + \lambda_j \mathsf{K}_G)\, \boldsymbol{\phi}_j = \mathsf{0}, \quad j \in \mathbb{N}_n. \tag{3.17}$$

The generalized eigenvalue problem (3.17) is solved for the eigenpairs $(\lambda_j, \boldsymbol{\phi}_j) \in (\mathbb{R} \times \mathbb{R}^n)$, where $\boldsymbol{\phi}_j$ is the buckling modeshape associated with the buckling load factor λ_j. Bathe (2006) argues that the accuracy of the (3.17) assumption is limited by the assumption of small pre-buckling displacements.

The one point approach mitigates this limitation by capturing finite deformations occurring before buckling in the aforementioned linearized buckling analysis (Brendel and Ramm (1980)). To this end, the equilibrium path is first traversed up until a predefined load level $\lambda^{\text{op}} \in \mathbb{R}$, using the general hyperelastic framework described in Sec. 2.1. In this deformed equilibrium position, a linearized buckling analysis similar to (3.17) is performed, but wherein $\mathsf{K}_L \rightarrow \mathsf{K}_o(\mathsf{u})$ and $\mathsf{K}_G \rightarrow \mathsf{K}_g(\mathsf{u})$, i.e.

$$(\mathsf{K}_o + \pi_j \mathsf{K}_g)\, \boldsymbol{\phi}_j = \mathsf{0}, \quad j \in \mathbb{N}_n, \tag{3.18}$$

is solved for the eigenpairs $(\pi_j, \boldsymbol{\phi}_j) \in (\mathbb{R} \times \mathbb{R}^n)$. The critical load factor is subsequently obtained as $\lambda^c = \min_{j \in \mathbb{N}_n} \pi_j \lambda^{\text{op}}$. The $\mathsf{K} = \mathsf{K}_o + \pi_j \mathsf{K}_g$ decomposition of the stiffness matrix is motivated by e.g. Wriggers (2008), and the explicit formats of K_o and K_g appear in Paper B.

Albeit the one point approach suffers from approximation errors which the extended system approach lacks, its simplicity and sufficient accuracy has made it a popular choice when probing for critical points. The one point approach also has the advantage of providing approximations of multiple critical point, which ultimately makes it the superior method for gradient-based optimization, cf. Paper B.

3.3 Elastic wave propagation

The elastic wave propagation properties of a pre-strained body is governed by (3.7), which is restated here using an operator form

$$\mathcal{A}(\boldsymbol{\phi}) = -\omega^2 \boldsymbol{\phi} \ \text{ in } \ \Omega, \tag{3.19}$$

where $\mathcal{A}(\boldsymbol{\phi}) = \frac{1}{\rho}\boldsymbol{\nabla} \cdot [\boldsymbol{L} : \boldsymbol{\nabla}\boldsymbol{\phi}]$. The body Ω, is assumed to consist of a heterogeneous material with a periodic microstructure, cf. Sec. (2.2). The aim is to solve (3.19) in the reduced space of the unit cell Ω^{μ}, but retain the solutions as if (3.19) was solved over Ω.

3.3.1 The reciprocal lattice

It is assumed that the periodic microstructure is a lattice structure, which is tessellated by rectangular unit cells with primitive lattice vectors $\boldsymbol{A}_1 = a_1\boldsymbol{e}_1$ and $\boldsymbol{A}_2 = a_2\boldsymbol{e}_2$. The periodicity manifests itself via the lattice's translational symmetry with respect to the lattice vectors $\boldsymbol{R} \in \mathcal{R} = \{\boldsymbol{R} \in \mathbb{R}^2 : \boldsymbol{R} = a\boldsymbol{A}_1 + b\boldsymbol{A}_2, \text{ for } (a,b) \in (\mathbb{N} \times \mathbb{N})\}$. Any function $f : \Omega \to \mathbb{R}$ which is spatially periodic in the lattice, satisfies

$$f(\boldsymbol{X}) = f(\boldsymbol{X} + \boldsymbol{R}). \tag{3.20}$$

It can be shown that functions which satisfy (3.20), can be defined in another space called the *reciprocal lattice*. To this end, f is expanded in a Fourier series

$$f(\boldsymbol{X}) = \sum_{\boldsymbol{\xi}} f_{\boldsymbol{\xi}} e^{i\boldsymbol{\xi}\cdot\boldsymbol{X}}, \tag{3.21}$$

where $e^{i\boldsymbol{\xi}\cdot\boldsymbol{X}}$ are plane waves with wave vectors $\boldsymbol{\xi} \in \mathbb{R}^2$. The condition (3.20) requires

$$f(\boldsymbol{X}) = \sum_{\boldsymbol{\xi}} f_{\boldsymbol{\xi}} e^{i\boldsymbol{\xi}\cdot\boldsymbol{X}} = f(\boldsymbol{X} + \boldsymbol{R}) = \sum_{\boldsymbol{\xi}} f_{\boldsymbol{\xi}} e^{i\boldsymbol{\xi}\cdot(\boldsymbol{X}+\boldsymbol{R})}, \tag{3.22}$$

or equivalently

$$\sum_{\boldsymbol{\xi}} f_{\boldsymbol{\xi}} e^{i\boldsymbol{\xi}\cdot\boldsymbol{X}} \left(1 - e^{i\boldsymbol{\xi}\cdot\boldsymbol{R}}\right) = 0. \tag{3.23}$$

Therefore, it is concluded that $f_{\boldsymbol{\xi}} = 0$ must hold for all $\boldsymbol{\xi}$ *except* for those $\boldsymbol{\xi}$ where $e^{i\boldsymbol{R}\cdot\boldsymbol{\xi}} = 1$ for all $\boldsymbol{R} \in \mathcal{R}$. Those vectors $\boldsymbol{\xi}$ which fulfill $e^{i\boldsymbol{R}\cdot\boldsymbol{\xi}} = 1$, or equivalently $\boldsymbol{R}\cdot\boldsymbol{\xi} = 2\pi N$ for all $N \in \mathbb{N}$, are denoted the reciprocal lattice vectors $\boldsymbol{G} = a\boldsymbol{B}_1 + b\boldsymbol{B}_2$ for $(a,b) \in (\mathbb{N} \times \mathbb{N})$. Hence the only non-vanishing terms of (3.21) are

$$f(\boldsymbol{X}) = \sum_{\boldsymbol{G}} f_{\boldsymbol{G}} e^{i\boldsymbol{G}\cdot\boldsymbol{X}}, \tag{3.24}$$

and the primitive reciprocal lattice vectors in two-dimensions are

$$\boldsymbol{B}_1 = 2\pi \frac{\boldsymbol{A}_2 \times \boldsymbol{e}_3}{\|\boldsymbol{A}_1 \times \boldsymbol{A}_2\|}, \quad \boldsymbol{B}_2 = 2\pi \frac{\boldsymbol{e}_3 \times \boldsymbol{A}_1}{\|\boldsymbol{A}_1 \times \boldsymbol{A}_2\|}, \tag{3.25}$$

such that $\boldsymbol{A}_k \cdot \boldsymbol{B}_l = 2\pi\delta_{kl}$, with $\boldsymbol{e}_3 = \frac{\boldsymbol{A}_1 \times \boldsymbol{A}_2}{\|\boldsymbol{A}_1 \times \boldsymbol{A}_2\|}$. An example of a square lattice in real and reciprocal space appears in Fig. 3.1.

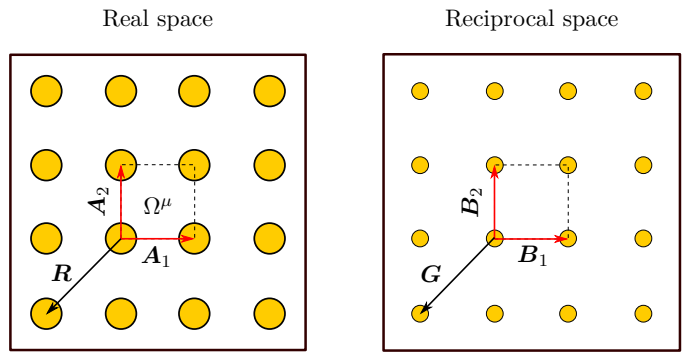

Fig. 3.1: A side length a square lattice in real space with primitive lattice vectors $\boldsymbol{A}_1 = a\boldsymbol{e}_1$ and $\boldsymbol{A}_2 = a\boldsymbol{e}_2$ (a) and in reciprocal space with reciprocal lattice vectors $\boldsymbol{B}_1 = \frac{2\pi}{a}\boldsymbol{e}_1$ and $\boldsymbol{B}_2 = \frac{2\pi}{a}\boldsymbol{e}_2$ (b). An unit cell Ω^μ is shown in dashed lines.

3.3.2 The Bloch form

Now, let us turn back to (3.19). Since the lattice is defined to be translational symmetric with respect to the lattice vectors $\boldsymbol{R} \in \mathcal{R}$, it holds that

$$\mathcal{T}_{\boldsymbol{R}}\mathcal{A}(\boldsymbol{\phi}(\boldsymbol{X})) = \mathcal{A}(\mathcal{T}_{\boldsymbol{R}}\boldsymbol{\phi}(\boldsymbol{X})), \tag{3.26}$$

where

$$\mathcal{T}_{\boldsymbol{R}}\boldsymbol{\phi}(\boldsymbol{X}) = \boldsymbol{\phi}(\boldsymbol{X} + \boldsymbol{R}), \tag{3.27}$$

is the translation operator in the direction of $\boldsymbol{R} \in \mathcal{R}$. Relation (3.26) shows that $\mathcal{A}$ and $\mathcal{T}_{\boldsymbol{R}}$ commute. The implication of the (3.26) relation becomes evident using (3.19), i.e.

$$\mathcal{T}_{\boldsymbol{R}}\mathcal{A}(\boldsymbol{\phi}(\boldsymbol{X})) = \mathcal{T}_{\boldsymbol{R}}(-\omega^2\boldsymbol{\phi}(\boldsymbol{X})) = -\omega^2\mathcal{T}_{\boldsymbol{R}}\boldsymbol{\phi}(\boldsymbol{X}) = \mathcal{A}(\mathcal{T}_{\boldsymbol{R}}\boldsymbol{\phi}(\boldsymbol{X})), \tag{3.28}$$

which shows that $(-\omega^2, \mathcal{T}_{\boldsymbol{R}}\boldsymbol{\phi}(\boldsymbol{X}))$ is another eigenpair of $\mathcal{A}$. Since the eigenvectors $\boldsymbol{\phi}(\boldsymbol{X})$ and $\mathcal{T}_{\boldsymbol{R}}\boldsymbol{\phi}(\boldsymbol{X})$ share the same eigenvalue, they must be parallel[9]

$$\mathcal{T}_{\boldsymbol{R}}\boldsymbol{\phi}(\boldsymbol{X}) = \alpha(\boldsymbol{R})\boldsymbol{\phi}(\boldsymbol{X}), \tag{3.29}$$

which is an eigenvalue problem of the operator $\mathcal{T}_{\boldsymbol{R}}$ with the eigenpairs $(\alpha, \boldsymbol{\phi}) \in (\mathbb{R} \times \mathbb{R}^2)$. This shows that the eigenvectors $\boldsymbol{\phi}$ which solve (3.19), also solve (3.29), i.e. $\mathcal{A}$ and $\mathcal{T}_{\boldsymbol{R}}$ share the same eigenspace, which is an inherent property of commutative operators.

Now, the aim is to find a general format of α in (3.29). Applying another $\mathcal{T}_{\boldsymbol{R}'}$ in the direction $\boldsymbol{R}' \in \mathcal{R}$ to (3.29) yields

$$\mathcal{T}_{\boldsymbol{R}'}\mathcal{T}_{\boldsymbol{R}}\boldsymbol{\phi}(\boldsymbol{X}) = \alpha(\boldsymbol{R})\mathcal{T}_{\boldsymbol{R}'}\boldsymbol{\phi}(\boldsymbol{X}) = \alpha(\boldsymbol{R})\alpha(\boldsymbol{R}')\boldsymbol{\phi}(\boldsymbol{X}), \tag{3.30}$$

[9] If $-\omega^2$ is degenerate, the eigenvectors $\boldsymbol{\phi}$ that solve (3.29) are in the span of the eigenvectors of $\mathcal{A}$, and vice versa.

but

$$\mathcal{T}_{\boldsymbol{R}'}\mathcal{T}_{\boldsymbol{R}}\boldsymbol{\phi}(\boldsymbol{X}) = \mathcal{T}_{\boldsymbol{R}'+\boldsymbol{R}}\boldsymbol{\phi}(\boldsymbol{X}) = \alpha(\boldsymbol{R}+\boldsymbol{R}')\boldsymbol{\phi}(\boldsymbol{X}), \tag{3.31}$$

must also hold following the definition of the translation operator. Therefore it is concluded that

$$\alpha(\boldsymbol{R}+\boldsymbol{R}') = \alpha(\boldsymbol{R})\alpha(\boldsymbol{R}'). \tag{3.32}$$

The format of $\alpha(\boldsymbol{R})$ that satisfies (3.32) is

$$\alpha(\boldsymbol{R}) = e^{i\boldsymbol{k}\cdot\boldsymbol{R}}, \tag{3.33}$$

where $\boldsymbol{k} \in \mathbb{R}^2$ is the so-called wave vector which classifies the solutions[10]. This implies that (3.29) becomes

$$\mathcal{T}_{\boldsymbol{R}}\boldsymbol{\phi}(\boldsymbol{X}) = \boldsymbol{\phi}(\boldsymbol{X})e^{i\boldsymbol{k}\cdot\boldsymbol{R}}, \tag{3.34}$$

which is the classical Bloch condition (Kittel (1976), Joannopoulos et al. (2011)). One format of $\boldsymbol{\phi}(\boldsymbol{X})$ which satisfy the (3.34) condition, is the Floquet-Bloch form, i.e.

$$\boldsymbol{\phi}(\boldsymbol{X}) = \boldsymbol{\phi}_p(\boldsymbol{X})e^{i\boldsymbol{k}\cdot\boldsymbol{X}}, \tag{3.35}$$

where $\boldsymbol{\phi}_p$ is translational symmetric with respect to $\boldsymbol{R}$, i.e.

$$\boldsymbol{\phi}_p(\boldsymbol{X}+\boldsymbol{R}) = \boldsymbol{\phi}_p(\boldsymbol{X}). \tag{3.36}$$

The Floquet–Bloch form (3.35) implies that the solutions to (3.19) takes the form of a plane wave $e^{i\boldsymbol{k}\cdot\boldsymbol{X}}$ which propagates in the direction described by the wave vector $\boldsymbol{k}$, and is modulated by a periodic function $\boldsymbol{\phi}_p(\boldsymbol{X})$.

3.3.3 The Brillouin zone

The remaining question is which $\boldsymbol{k}$ that necessitates interrogation when solving (3.19). This is investigated by utilizing the (3.24) result on $\boldsymbol{\phi}_p$, wherefore (3.35) becomes

$$\boldsymbol{\phi}(\boldsymbol{X}) = \sum_{\boldsymbol{G}} \boldsymbol{\phi}_{p,\boldsymbol{G}}e^{i(\boldsymbol{k}+\boldsymbol{G})\cdot\boldsymbol{X}}, \tag{3.37}$$

which shows that the wave vectors are described in reciprocal space, i.e. $\boldsymbol{k} = k_1\boldsymbol{B}_1 + k_2\boldsymbol{B}_2$. Since the sum in (3.37) is over all possible reciprocal lattice vectors $\boldsymbol{G}$, it makes no sense that $\boldsymbol{k}$ should include any integer multiples of $\boldsymbol{G}$. Therefore, the space in which $\boldsymbol{k}$ is defined can be limited to the so-called 1st *Brillouin zone* (BZ), which is the smallest zone in the reciprocal space containing all non-redundant values of $\boldsymbol{k}$. The same conclusion can be made by returning to (3.34) and setting $\boldsymbol{k} \to \boldsymbol{k}+\boldsymbol{G}$, wherefore

$$\mathcal{T}_{\boldsymbol{R}}\boldsymbol{\phi}(\boldsymbol{X}) = \boldsymbol{\phi}(\boldsymbol{X})e^{i(\boldsymbol{k}+\boldsymbol{G})\cdot\boldsymbol{R}} = \boldsymbol{\phi}(\boldsymbol{X})e^{i\boldsymbol{k}\cdot\boldsymbol{R}}e^{i\boldsymbol{G}\cdot\boldsymbol{R}} = \boldsymbol{\phi}(\boldsymbol{X})e^{i\boldsymbol{k}\cdot\boldsymbol{R}}, \tag{3.38}$$

i.e. $\boldsymbol{k}+\boldsymbol{G}$ describes the same eigenmode of $\mathcal{T}_{\boldsymbol{R}}$ as $\boldsymbol{k}$.

[10]The magnitude of the wave vector corresponds to the one-dimensional wave number.

If the lattice experiences additional rotation, reflection, and/or inversion symmetries, the space of $\boldsymbol{k}$ can be further reduced to the so-called *irreducible* Brillouin zone (IBZ). It is however crucial to remember that the applied deformation affects these symmetries, cf. Fig 2.2. Indeed, the lattice vectors in the current configuration, $\boldsymbol{a}_j$, are obtained via $\boldsymbol{a}_j = \boldsymbol{F}^M \cdot \boldsymbol{A}_j$, $j = 1, 2$ (Zhang and Parnell (2017)). However, if the applied macroscopic deformations are limited to those which retain domain symmetry with respect to reflections about the $\boldsymbol{e}_1$ and $\boldsymbol{e}_2$ axes, the IBZ of a square lattice becomes the first quadrant depicted in Fig. 3.2.

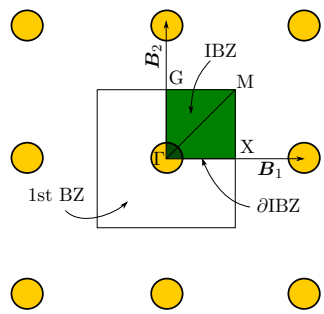

Fig. 3.2: Illustration of the 1st Brilliouin zone (BZ), the irreducible Brillouin zone (IBZ) and the boundary of the IBZ, (∂IBZ) for a square lattice in reciprocal space.

It is common to only interrogate a finite subset $\partial\mathcal{S}_k$ of the $\boldsymbol{k}$-vectors located on the boundary ∂IBZ of the IBZ, i.e.

$$\partial\mathcal{S}_k = \{\boldsymbol{k}_n \in \partial\text{IBZ},\ 1 \leq n \leq N_k\}, \tag{3.39}$$

where $\boldsymbol{k}_n$, $1 \leq n \leq N_k$ are the wave vectors along ∂IBZ and $N_k \in \mathbb{N}$ is the number of sampling points. However, Maurin et al. (2018) show via numerous examples that the band extrema may not be located on the boundary, and therefore the full IBZ must be probed to confirm the omnidirectionality of a bandgap.

3.3.4 One-dimensional example

To introduce the concept of elastic wave dispersion, the dynamical behavior of the periodic one-dimensional system presented by Jensen (2003), and depicted in Fig. 3.3, is investigated. The system compromises an infinite number of lumped masses m_n, separated a distance l_e via springs with stiffness k_n, $n \in \mathbb{N}_{1\text{D}} = \{1, 2, ..., \infty\}$. The system is periodic, i.e. is constituted by an infinite amount of identical unit cells, each L long and encompassing $N - 1$ number of masses and springs. The horizontal displacement in the discrete positions of the masses are quantified by u_n, $n \in \mathbb{N}_{1\text{D}}$.

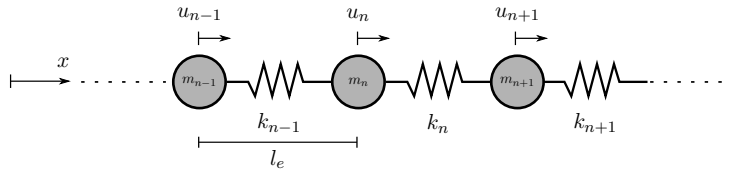

Fig. 3.3: The one dimensional mass-spring system.

The equations of motion of the n:th mass is

$$m_n \ddot{u}_n = k_n(u_{n+1} - u_n) - k_{n-1}(u_n - u_{n-1}), \quad n \in \mathbb{N}_{1D}, \tag{3.40}$$

assuming linear springs. Analogously to the (3.6) ansatz, it is assumed that

$$u_n(x,t) = \phi_n(x)e^{-i\omega t}, \tag{3.41}$$

wherefore (3.12) becomes

$$m_n\omega^2\phi_n = k_{n-1}(\phi_n - \phi_{n-1}) - k_n(\phi_{n+1} - \phi_n), \quad n \in \mathbb{N}_{1D}. \tag{3.42}$$

Obtaining the solutions ϕ_n for all degrees-of-freedom $n \in \mathbb{N}_{1D}$ via the assembly of (3.42) is evidently infeasible. Instead, the solutions can be obtained in a reduced space by taking advantage of system's spatial periodicity. To this end, the analysis of the Fig. 3.3 system is reduced to a single unit cell with periodic Bloch conditions, cf. Fig. 3.4.

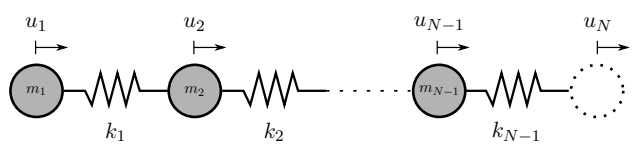

Fig. 3.4: An unit cell encompassing $N-1$ number of masses and springs.

In this way, the unit cell solutions to (3.42) are assumed to take Floquet-Bloch form, i.e.

$$\phi_j = \hat{\phi}_j e^{ik(j-1)l_e}, \quad j = 1, 2, ..., N \tag{3.43}$$

where $\hat{\phi}_j$ is spatially periodic and k is the wave number. Additionally, the (3.34) Bloch condition must be fulfilled, which is posed as

$$\phi_N = \phi_1 e^{ikL}, \tag{3.44}$$

in a master-slave implementation.

To illustrate the process of applying the Bloch boundary conditions, a unit cell with $N = 5$ degrees-of-freedoms is considered. The assembled system of equations (3.42) for the unit cell is

$$\underbrace{\begin{bmatrix} k_1 & -k_1 & 0 & 0 & 0 \\ -k_1 & k_1+k_2 & -k_2 & 0 & 0 \\ 0 & -k_2 & k_2+k_3 & -k_3 & 0 \\ 0 & 0 & -k_3 & k_3+k_4 & -k_4 \\ 0 & 0 & 0 & -k_4 & k_4 \end{bmatrix}}_{\mathsf{K}} \underbrace{\begin{bmatrix} \phi_1 \\ \phi_2 \\ \phi_3 \\ \phi_4 \\ \phi_5 \end{bmatrix}}_{\boldsymbol{\Phi}_j} = \omega_j^2 \underbrace{\begin{bmatrix} m_1 & 0 & 0 & 0 & 0 \\ 0 & m_2 & 0 & 0 & 0 \\ 0 & 0 & m_3 & 0 & 0 \\ 0 & 0 & 0 & m_4 & 0 \\ 0 & 0 & 0 & 0 & 0 \end{bmatrix}}_{\mathsf{M}} \underbrace{\begin{bmatrix} \phi_1 \\ \phi_2 \\ \phi_3 \\ \phi_4 \\ \phi_5 \end{bmatrix}}_{\boldsymbol{\Phi}_j} \tag{3.45}$$

The master-slave implementation of the Bloch boundary conditions proceeds via the condensation

$$\begin{bmatrix} \phi_1 \\ \phi_2 \\ \phi_3 \\ \phi_4 \\ \phi_5 \end{bmatrix} = \begin{bmatrix} 1 & 0 & 0 & 0 \\ 0 & 1 & 0 & 0 \\ 0 & 0 & 1 & 0 \\ 0 & 0 & 0 & 1 \\ e^{ikL} & 0 & 0 & 0 \end{bmatrix} \begin{bmatrix} \phi_1 \\ \phi_2 \\ \phi_3 \\ \phi_4 \end{bmatrix} \quad \Leftrightarrow \quad \boldsymbol{\Phi}_j = \mathsf{W}(k)\boldsymbol{\Phi}_j^\bullet, \tag{3.46}$$

wherefore (3.45) becomes

$$\mathsf{W}(k)^T\mathsf{K}\mathsf{W}(k)\boldsymbol{\Phi}_j^\bullet = \omega^2\mathsf{W}(k)^T\mathsf{M}\mathsf{W}(k)\boldsymbol{\Phi}_j^\bullet \quad \Leftrightarrow \quad \mathsf{K}^\bullet\boldsymbol{\Phi}_j^\bullet = \omega_j^2\mathsf{M}^\bullet\boldsymbol{\Phi}_j^\bullet, \tag{3.47}$$

if premultiplying by $\mathsf{W}(k)^T$[11].

Following Jensen (2003), the mass-spring system is assumed to discretize a $L = 0.15$ m rod consisting of PMMA (Young's modulus: $E_p = 5.28$ GPa, density: $\rho_p = 1200$ kg/m^3) and aluminum (Young's modulus: $E_a = 70.9$ GPa, density: $\rho_a = 2830$ kg/m^3). However, to facilitate the discussion, the discretization of a homogeneous aluminum rod is considered first. The $N = 5$ unit cell provides the dispersion diagram seen in Fig. 3.5(a) for $k = [0, 4\pi/L]$. Here, the redundancy of the k-values outside of the irreducible Brillouin zone BZ $= \{k \in [0, \pi/L]\}$ is visible. It is also noted that no gaps exist in the $\omega(k)$ relation. This is not very surprising, since a homogeneous medium is non-dispersive, i.e. the phase velocity $v_p = \frac{dw}{dk} = \sqrt{\frac{E}{\rho}}$ is constant, wherefore $w(k)$ exhibits a linear behavior. Indeed, the slope of the first band for $k = [0, \pi/L]$ is approximately v_p, and in the limit $N \to \infty$ a linear $w(k)$ will hold for all bands.

[11]The premultiplication by $\mathsf{W}(k)^T$ naturally appears if imposing the Bloch boundary conditions on the solutions to the weak form in the continuum setting.

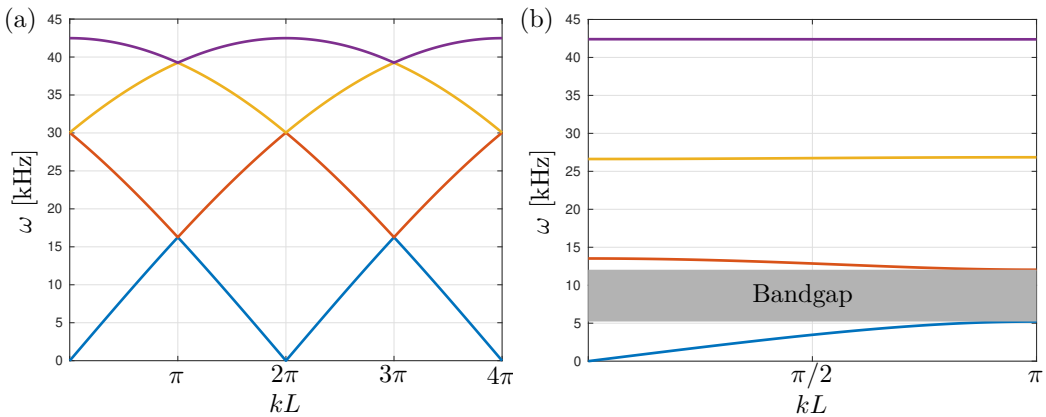

Fig. 3.5: The dispersion diagram for a (a) homogeneous aluminum rod and (b) heterogeneous PMMA/aluminum rod.

Next, a heterogeneous rod is considered. The rod's constituent is PMMA for $\frac{L}{4} \leq x \leq \frac{3L}{4}$, whereas the rest is aluminum, i.e. in total $L_a = \frac{L}{2}$ and $L_p = \frac{L}{2}$. The dispersion diagram for this rod appears in Fig. 3.5(b). Herein, multiple *bandgaps* appear, and the lowest frequency ω_1-ω_2 bandgap is indicated by a gray region. Any incoming wave with frequency ω within the range of a bandgap will not be able to propagate through the rod. The ω_1-ω_2 bandgap appears at the edge of the Brillouin zone, i.e. at $k = \frac{\pi}{L}$. The ϕ_1 and ϕ_2 modes at $k = \frac{\pi}{L}$ are depicted as transversal displacements of the masses in Fig. 3.6.

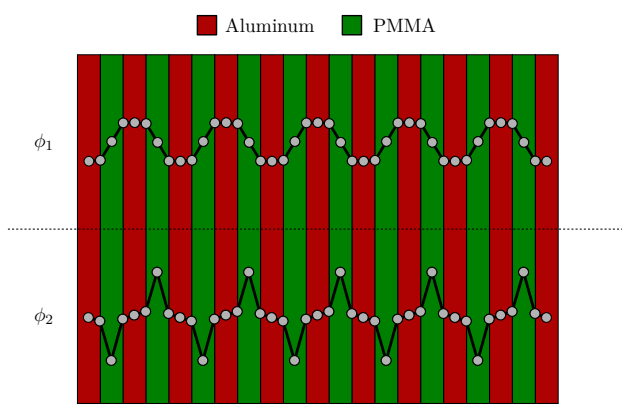

Fig. 3.6: The ϕ_1 and ϕ_2 mode for 10 heterogeneous unit cells at $k = \frac{\pi}{L}$.

To quantify the size of a bandgap, the so-called *gap-midgap* ratio is used, i.e.

$$B_b = \frac{\min\limits_k \omega_{b+1}(k) - \max\limits_k \omega_b(k)}{\min\limits_k \omega_{b+1}(k) + \max\limits_k \omega_b(k)}, \tag{3.48}$$

where b is the band index. The gap-midgap ratio increases as the contrast between the material parameters increases, as readily verified for B_1 in Fig. 3.7(a). In Fig. 3.7(b), B_1 is plotted against the length of the PMMA section in the unit cell. The maximum bandgap occurs for $L_p = 0.04425$ m, which is close to the theoretical maximum (≈ 0.04430), corresponding to a so-called *quarter-wave stack* or *Bragg reflector* (Joannopoulos et al. (2011)). To conclude, it is found that the size of the bandgaps can be controlled via the distribution and selection of the constituent materials in the unit cell.

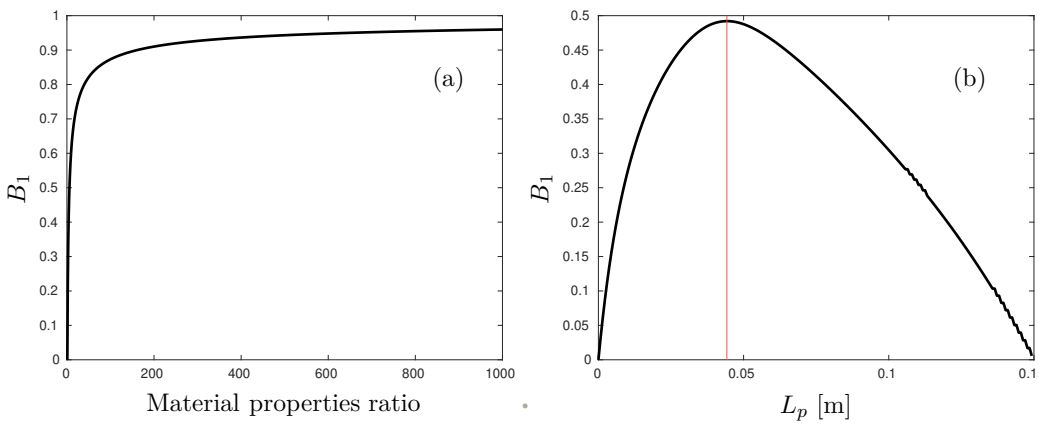

Fig. 3.7: The gap-midgap ratio versus (a) the material properties ratio and (b) the length of the PMMA section L_p in the unit cell. The unit cell is discretized by 200 elements, i.e. $N = 201$. In (a), the ratio is defined such that $E_1/E_2 = \rho_1/\rho_2$. The red line in (b) indicate the maximum value of B_1, which occurs for $L_p = 0.04425$ m and $L_a = 0.10575$.

4 Gradient-based optimization

This section provides a brief introduction to *topology* and *shape* gradient-based optimization. Both of these optimization problems are often ill-posed in their original formulation, which manifests itself via the lack of solutions. Therefore, techniques for obtaining well-posed optimization problems are presented. The traditional fictitious domain approach to topology optimization is scrutinized, wherein the discussion also involves various ways of improving the resolution of the design boundaries.

4.1 Topology optimization

Topology optimization aims to distribute material in a design domain Ω^d, such that a predefined objective is optimized subject to constraints. Although various approaches to topology optimization exist, such as; level-set (Allaire et al. (2002),Wang et al. (2003)), phase-field (Bourdin and Chambolle (2003), Wallin et al. (2015)) and topological derivative (Sokolowski and Zochowski (1999)), the typical topology optimization problem is *density*-based (Bendsøe (1989)), as in this thesis[12]. In the latter method, the integer field $d(\boldsymbol{X}) \in \{0, 1\}$ is introduced to quantify the material distribution, such that $d(\boldsymbol{X}) = 1$ or $d(\boldsymbol{X}) = 0$ if $\boldsymbol{X} \in \Omega^d$ should contain material or not. Unfortunately, the direct use of this integer field approach may render an ill-posed optimization problem which lacks solution, manifested via optimized designs that contain a non-converging series of microstructures (Bendsøe (1989), Sigmund and Petersson (1998)). This is especially prominent when maximizing the structural stiffness, since the introduction of additional void cavities generally improves this measure. The integer field approach is also problematic since standard gradient-based optimization methods cannot be used.

To obtain a well-posed topology optimization problem, *relaxation* or *restriction* of the design space can be employed. The principle of relaxation implies an enlargement of the design space, such that $d(\boldsymbol{X}) \in \{0, 1\}$ is replaced by a continuous field $z(\boldsymbol{X}) \in [0, 1]$. That z is continuous allows the optimization problem to be solved using gradient-based optimization methods. The only physically sound interpretation of the optimal distribution of a z field that linearly scales the material properties is a variable thickness sheet distribution problem (Cheng and Olhoff (1981), Bendsøe and Sigmund (1999)). For problems where the material properties instead depend non-linearly on z, the regions with intermediate $z \in (0, 1)$ may be physically interpreted as microstructures, and their effective properties can be obtained via homogenization (Bendsøe and Kikuchi (1988), Groen and Sigmund (2018)). In practice, the optimized designs obtained by relaxation might be difficult to manufacture.

Restriction implies that the solution to the topology optimization problem is sought for in a design space which is smaller than the original space. This is accomplished by introducing constraints that bound the maximum allowed spatial oscillations of d, for example in the form of perimeter control (Haber et al. (1996)). However, since d remains an integer field, special solvers for integer programming problems must be used. Therefore, it is common to resort to penalization methods such as the Simple Isotropic Material with Penalization (SIMP) method (Bendsøe (1989)), wherein a continuous design variable field, $z(\boldsymbol{X}) \in [0, 1]$, is used while simultaneously penalizing

[12]The following discussion will mainly focus on the density-based approach. Exhaustive reviews of other methods appear in e.g. Sigmund and Maute (2013) and Deaton and Grandhi (2014).

intermediate densities in hope of approaching a binary design. To obtain a well-posed optimization problem, the spatial oscillations of z are regularized via e.g. slope constraints (Petersson and Sigmund (1998)), sensitivity filtering (Sigmund (1994)) or design field filtering (Bruns and Tortorelli (2001), Bourdin (2001)). The topology optimization methods presented in this thesis utilize penalization in combination with filtering to obtain a well-posed optimization problem.

4.1.1 Filtering

Filtering methods aim to regularize the spatial oscillations of $z(\boldsymbol{X}) \in [0,1]$ by imposing a length-scale. A commonly used filter is the convolution filter, sometimes referred to as the *density* filter (Bruns and Tortorelli (2001), Bourdin (2001)). In this method, z is replaced by the filtered field $\nu : \Omega^d \to [0,1]$, obtained as a weighted average of $z(\boldsymbol{X})$

$$\nu(\boldsymbol{X}) = \frac{\displaystyle\int_{\Omega^r(\boldsymbol{X})} k(\boldsymbol{X}-\boldsymbol{Y}) z(\boldsymbol{Y})\, d\boldsymbol{Y}}{\displaystyle\int_{\Omega^r(\boldsymbol{X})} k(\boldsymbol{X}-\boldsymbol{Y})\, d\boldsymbol{Y}}, \tag{4.1}$$

where $\Omega^r(\boldsymbol{X}) \subseteq \Omega^d$ is a circle of radius $r > 0$ centered at $\boldsymbol{X}$ and k is a suitable kernel, cf. Bourdin (2001). In Paper A, k is the cone filter function $k(\boldsymbol{X}) = \max(0, 1 - \|\boldsymbol{X}\|_2 / l)$, where $l > 0$ is the length-scale which controls the smoothness of ν.

An alternative, implicit, formulation of the convolution filter is obtained as a solution to the PDE

$$-l^2 \boldsymbol{\nabla}^2 \nu + \nu = z, \tag{4.2}$$

together with appropriate boundary conditions, cf. Lazarov and Sigmund (2011). The solutions to (4.2) are similar to (4.1), except that the filter function k is replaced by Green's function, cf. Lazarov and Sigmund (2011). The PDE (4.2) is traditionally solved subject to the homogeneous Neumann condition $\boldsymbol{\nabla}\nu \cdot \boldsymbol{n}_d = 0$ on $\partial\Omega^d$, where $\boldsymbol{n}_d$ is the unit normal to $\partial\Omega^d$. This causes the design's boundaries to be perpendicular to the domain edges $\partial\Omega^d$. Other possible boundary conditions exist, which models different boundary effects (Clausen and Andreassen (2017), Wallin et al. (2020)). Those $\nu \in \{\nu \in H^1 : \boldsymbol{\nabla}\nu(\boldsymbol{X}) \cdot \boldsymbol{n}_d = 0 \text{ for } \boldsymbol{X} \in \partial\Omega^d\}$ that satisfy (4.2), must also fulfill the weak form

$$\delta r_\nu(\nu; \delta\nu) := \int_{\Omega^d} l^2 \boldsymbol{\nabla}\nu \boldsymbol{\nabla}\delta\nu \, dV - \int_{\Omega^d} (\nu - z)\delta\zeta \, dV = 0, \tag{4.3}$$

for all smooth admissible $\delta\nu$.

4.1.2 Material interpolation

As indicated by the name of the *density*-based topology optimization method, the continuous and filtered ν field could be seen as a dimensionless "density" which scales the material properties in each $\boldsymbol{X} \in \Omega^d$. If the final design predominantly contains the extreme values of ν, i.e. $\nu \in \{0,1\}$, it could be argued that the limited regions containing intermediate $\nu \in (0,1)$ should not affect the global behavior, at least for maximum stiffness problems. Hence, the interpolation of the material properties

with respect to ν must not coincide with a physically realizable microstructure. The extensively used SIMP interpolation (Bendsøe (1989)), applied to the Young's modulus of the constituent material phase E_o

$$E(\nu) = (\delta_o + (1 - \delta_o)\,\nu^p)\,E_o \;\text{ where }\; \delta_o \ll 0, \tag{4.4}$$

is part of the group of interpolations which violate the Hashin-Shtrikman bounds (Hashin and Shtrikman (1963)) for certain choices of penalization parameter $p > 0$ (Bendsøe and Sigmund (1999)). Nonetheless, it is one of the most commonly employed interpolation, probably due to its simplicity and the aforementioned reasoning. The idea behind the $p > 1$ SIMP interpolation (4.4), is that the stiffness-to-mass ratio is reduced for $\nu \in (0, 1)$, wherefore it is "uneconomical" for the optimizer to utilize intermediate densities when maximizing the stiffness subject to a maximum volume constraint[13]. Alternatives to (4.4) do exist. For example, the Rational Approximation of Material Properties (RAMP) interpolation (Stolpe and Svanberg (2001))

$$E(\nu) = \left(\delta_o + \frac{\nu\,(1 - \delta_o)}{1 + q\,(1 - \nu)}\right) E_o, \tag{4.5}$$

is a popular choice due to its non-vanishing derivative at $\nu = 0$ for all $q > 0$. The SIMP and RAMP interpolations appear in Fig. 4.1.

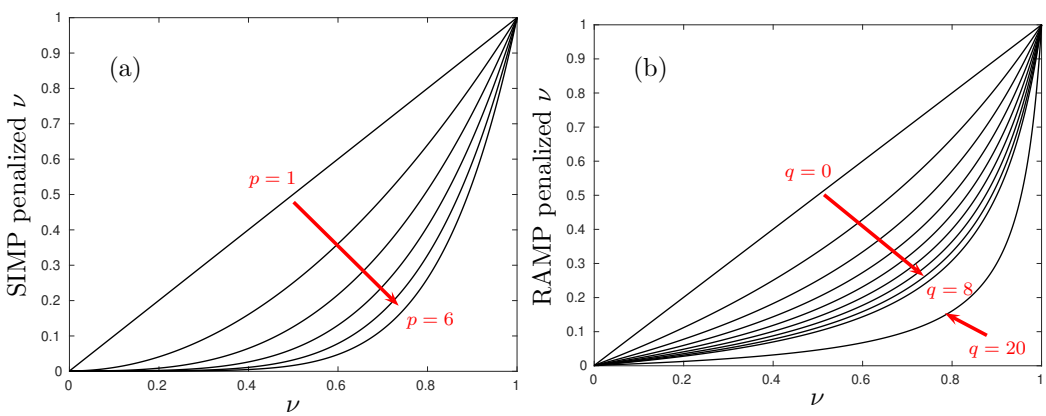

Fig. 4.1: The (a) SIMP and (b) RAMP interpolations versus ν. Here, $\delta_o = 10^{-3}$, cf. (4.4) and (4.5).

4.2 Boundary representation

The filtering invariably results in regions wherein $\nu \in (0, 1)$. This effect is especially prominent along design boundaries, leading to a non-unique design definition which obstructs its realization. Additionally, these blurry interfaces might complicate the application of design dependent boundary conditions and render non-physical structural behavior such as premature yielding (Maute et al. (1998), Makhija and Maute (2014)). One way of addressing this issue is to arbitrarily choose a threshold at

[13] Traditionally, the physical density is scaled linearly with respect to ν.

which to extract the design representation, and in a post-processing step perform a shape optimization in hope of finding the optimal design shape. This approach is investigated in Paper D. However, for certain optimization problems where accurate boundary representations are crucial to correctly characterize the physics, as is the case in e.g. phononic crystal design (Sigmund and Søndergaard Jensen (2003)) or fluid-structure interaction problems (Yoon (2010b)), the aforementioned approach might yield sub-optimal designs.

4.2.1 Projection

In density-based topology optimization it is common to project the filtered design field onto an smoothed Heaviside step function, $H_{\beta,\eta} : \mathbb{R} \to [0, 1]$, such that the extent of the $\nu \in (0, 1)$ regions are limited, cf. Guest et al. (2004). One version of $H_{\beta,\eta}$ is (Wang et al. (2014))

$$\bar{\nu} = H_{\beta,\eta}(\nu) = \frac{\tanh(\beta\eta) + \tanh(\beta(\nu - \eta))}{\tanh(\beta\eta) + \tanh(\beta(1 - \eta))}, \tag{4.6}$$

where $\bar{\nu}$ is the filtered and projected design variable field, and $(\beta, \eta) \in (\mathbb{R} \times \mathbb{R})$ are numerical parameters defined such that $\lim_{\beta\to\infty} H_{\beta,\eta}(\nu) = u_s(\nu - \eta)$, where u_s is the unit step function. By filtering and subsequently projecting the design field with a large value of β, the density-based topology optimization approach becomes similar to an ersatz material level-set approach, cf. Sigmund and Maute (2013) and Andreasen et al. (2020). In practice, it is common to utilize a continuation scheme on β during the optimization iterations, which reduces the likelihood of convergence to local optimas.

Even though the design boundaries might be "crisp" as a result of the projection operation, they are most likely poorly resolved due to misalignment with the computational mesh. To mitigate this issue, Wallin et al. (2012) and Salazar de Troya and Tortorelli (2018) introduce adaptive mesh refinement, which improves the resolution of the interfaces. Another possibility is to repeatedly generate body fitted meshes during the optimization iterations, such that the structural boundaries always align with the computational mesh, cf. e.g. Maute and Ramm (1995) and Xia et al. (2012). Unfortunately, the re-meshing strategies might affect the convergence rate of a gradient-based optimization due to inconsistent sensitivity information (Schleupen et al. (2000)), in addition to increasing the computational cost. Andreasen et al. (2020) instead address the issue using the cut-element method, which result in an increased accuracy in the interface integration. This method is however unable to capture discontinuities in the interpolated fields, which leads to spurious couplings between the material phases. To accurately characterize the discontinuity of transitioning between material phases, the eXtended Finite Element Method (XFEM) (Makhija and Maute (2014)) or CutFEM (Villanueva and Maute (2017), Burman et al. (2019)) with a suitable enrichment strategy could be used.

4.2.2 Shape optimization

This thesis is mainly concerned with the density-based topology optimization. However, in Papers D and E, a shape optimization approach is also considered, wherefore a presentation of this subject is relevant. In fact, the optimization of the filtered and projected[14] design field, or the similar

[14]Assuming $\beta \gg 1$, cf. (4.6).

level-set representation, can be argued to be akin to a shape optimization method in the sense that new holes do not naturally appear since the non-vanishing sensitivities are limited to the interface regions. As previously discussed, both density and level-set methods are traditionally based on an Eulerian approach, i.e. the parameterized design is projected on a fixed background mesh. The conventional shape optimization is instead based on a Lagrangian approach, wherein a conforming mesh is generated over the design configuration, wherefore the optimization is devoted to changing the position and shape of the domain boundaries. The Lagrangian approach to shape optimization result in explicit descriptions of the structural boundaries, solely limited by the mesh resolution.

One of the earliest approaches to shape optimization was to use the finite element nodal coordinates on the design domain's boundaries as design variables (Zienkiewicz and Campbell (1973)). Analogously to the ill-posedness of the integer field approach to topology optimization, this approach results in the non-existence of solutions, manifested via designs that contain infinitely fine oscillating boundaries (Chenais (1975), Le et al. (2011)). Again, a well-posed shape optimization problem is obtained via restriction of the design space by introducing a length scale on the solution, e.g. by parameterizing the shape (Braibant and Fleury (1984)) or by filtering (Le et al. (2011)). Comprehensives reviews of shape optimization methods appear in e.g. Haftka and Grandhi (1986) or Sigmund and Maute (2013).

Inspired by the variable nodal coordinate approach to shape optimization, Belegundu and Rajan (1988) introduce the so-called natural design variable method. In this method, the design variables are external forces on the domain boundaries, and a linear elasticity shape change problem is solved to "deform" the design into the optimal configuration. Since the mesh is morphed to comply with the shape changes, re-meshing should not be needed. This approach enforces a length-scale on the solution, leading to a well-posed shape optimization problem. A similar approach is proposed by Scherer et al. (2010), where prescribed displacements rather than loads are the design variables. To regularize the problem, a hyperelastic shape change problem is solved, which allows the finite elements to rotate, translate and dilate, but which penalizes shearing and stretching. To control mesh distortion, an upper bound on the energy of the shape change analysis is enforced. Recently, Swartz et al. (2023) compared the linear elastic and non-linear hyperelastic "filters", and found that a trade-off between superior mesh quality (hyperelastic filters) and computational efficiency (linear elastic filters) existed.

In Papers D and E, a filter similar to the *fictitious energy approach* developed by Scherer et al. (2010) is used. This filter is also based on the solution to a hyperelastic shape change problem. In this filtration, $\boldsymbol{s}$ governs the smoothed design displacement $\boldsymbol{\psi}$ resulting from the application of a Robin boundary condition involving $\boldsymbol{s}$ to $\partial\Omega_o^s$, where $\partial\Omega_o^s$ are the structural boundaries which are subject to the shape optimization. In this way, we have $\Omega = \boldsymbol{\varphi}_\psi(\Omega_o)$ and $\boldsymbol{\varphi}_\psi(\boldsymbol{X}_o) = \boldsymbol{X}_o + \boldsymbol{\psi}(\boldsymbol{X}_o)$. It is assumed that $\boldsymbol{\psi}$ is found from the minimization of the fictitious potential

$$\Pi_\psi(\boldsymbol{\psi}) = \int_{\Omega_o} W_\psi \, dV + \frac{1}{2}\int_{\partial\Omega_o^s} ||\boldsymbol{\psi} - \boldsymbol{s}||^2 \, dS, \tag{4.7}$$

where W_ψ is a fictitious hyperelastic strain energy[15]. The equilibrium configurations of (4.7) are

[15]The $(\,\cdot\,)_\psi$ notation is used to indicate variables that are associated with $\boldsymbol{\psi}$.

defined as those smooth admissible $\delta\boldsymbol{\psi}$ which satisfy

$$\delta\Pi_{\psi}(\boldsymbol{\psi};\delta\boldsymbol{\psi}) = \int_{\Omega_o} \boldsymbol{P}_{\psi} : \boldsymbol{\nabla}\delta\boldsymbol{\psi}\, dV + \int_{\partial\Omega_o^s} (\boldsymbol{\psi} - \boldsymbol{s}) \cdot \delta\boldsymbol{\psi}\, dS = 0, \tag{4.8}$$

where $\boldsymbol{P}_{\psi} = \frac{\partial W_{\psi}}{\partial \boldsymbol{\nabla}\boldsymbol{\psi}}$ follows from the hyperelastic assumption. From (4.8), the local balance equations can be extracted by utilizing the product rule and the divergence theorem in combination with the arbitrariness of $\delta\boldsymbol{\psi}$,

$$\begin{aligned} &\boldsymbol{\nabla}\cdot\boldsymbol{P}_{\psi} = \boldsymbol{0}, \quad \text{in} \quad \Omega_o, \\ &\boldsymbol{P}_{\psi}\cdot\boldsymbol{n} = \boldsymbol{s} - \boldsymbol{\psi}, \quad \text{on} \quad \partial\Omega_o^s. \end{aligned} \tag{4.9}$$

It is emphasize that the boundary condition is of Robin type, through which the design variable field $\boldsymbol{s}$ drives $\boldsymbol{\psi}$.

The weak form (4.8) is solved using finite element approximations of $\boldsymbol{s}$ and $\boldsymbol{\psi}$. Using the arbitrariness of $\delta\boldsymbol{\psi}$, the discretized residual becomes

$$\mathsf{r}_{\psi}(\boldsymbol{\nu}) = \sum\!\!\!\!\!\!\int_{\Omega_o} (\boldsymbol{\nabla}\mathsf{N})^T \mathsf{P}_{\psi}\, dV - \sum\!\!\!\!\!\!\int_{\partial\Omega_o^s} \mathsf{N}^T\,(\boldsymbol{s} - \boldsymbol{\psi})\; dS = \boldsymbol{0}. \tag{4.10}$$

The balance equations (4.10) constitutes a nonlinear relation between $\boldsymbol{s}$ and $\boldsymbol{\psi}$, wherefore they are solved via linearization, i.e.

$$\mathsf{r}_{\psi}(\boldsymbol{\psi} + d\boldsymbol{\psi}) = \mathsf{r}_{\psi}(\boldsymbol{\psi}) + \frac{\partial \mathsf{r}_{\psi}}{\partial \boldsymbol{\psi}} d\boldsymbol{\psi} = \boldsymbol{0} \quad \Leftrightarrow \quad \mathsf{K}_{\psi} d\boldsymbol{\psi} = -\mathsf{r}_{\psi}, \tag{4.11}$$

which is solved iteratively until convergence, i.e. $\boldsymbol{\psi} \leftarrow \boldsymbol{\psi} + d\boldsymbol{\psi}$ until $\|\mathsf{r}_{\psi}\| \approx 0$.

To see that the $\boldsymbol{\psi}$ field is smoother than $\boldsymbol{s}$, i.e. that fine-scale oscillations of $\boldsymbol{s}$ are limited via (4.7), the spectral decomposition of K_{ψ} is introduced as[16]

$$\mathsf{K}_{\psi}\boldsymbol{\Phi} = \boldsymbol{\Phi}\boldsymbol{\Lambda} \quad \Leftrightarrow \quad \mathsf{K}_{\psi} = \boldsymbol{\Phi}\boldsymbol{\Lambda}\boldsymbol{\Phi}^T, \tag{4.12}$$

where $\boldsymbol{\Phi} = [\boldsymbol{\phi}_1, \boldsymbol{\phi}_2, ..., \boldsymbol{\phi}_n]$ are the eigenvectors which are normalized such that $\boldsymbol{\phi}_j^T\boldsymbol{\phi}_l = \delta_{jl}$ and $\boldsymbol{\Lambda}$ is a diagonal matrix which contains the eigenvalues λ_j, $j \in \mathbb{N}_n$ ordered in ascending order. By assuming that K_{ψ} is positive definite (i.e. $\lambda_j > 0$, $j \in \mathbb{N}_n$), and inserting the spectral decomposition (4.12) in (4.11), it is found that

$$\boldsymbol{\Phi}\boldsymbol{\Lambda}\boldsymbol{\Phi}^T d\boldsymbol{\psi} = -\mathsf{r}_{\psi} \quad \Leftrightarrow \quad d\boldsymbol{\psi} = -\boldsymbol{\Phi}\boldsymbol{\Lambda}^{-1}\boldsymbol{\Phi}^T\mathsf{r}_{\psi} = -\sum_{j=1}^{n} \frac{1}{\lambda_j}\boldsymbol{\phi}_j\left(\boldsymbol{\phi}_j^T\mathsf{r}_{\nu}\right), \tag{4.13}$$

where $n = \max(\mathbb{N}_n)$. Inspecting (4.13), it appears that the smallest magnitude eigenpairs $(\lambda_j, \boldsymbol{\phi}_j)$ contribute the most to $d\boldsymbol{\psi}$, which indicates that (4.3) acts similar to a low-pass filter.

[16]Since K_{ψ} is real and symmetric, $\boldsymbol{\Phi}$ is unitary, i.e. $\boldsymbol{\Phi}^T = \boldsymbol{\Phi}^{-1}$.

4.3 Fictitious domain

As previously mentioned, the traditional topology optimization method is based on an Eulerian approach, wherein the parameteried design is project on a fixed background mesh. This is also referred to as a *fictitious domain* approach. The material distribution is quantified by the continuous filtered field $\nu \in [0,1]$, such that if $\nu(\boldsymbol{X}) = 1$ the material point $\boldsymbol{X} \in \Omega^d$ contains material, and if $\nu(\boldsymbol{X}) = 0$ the material point lacks material, i.e. characterizes void. However, "true" void cannot exist in an Eulerian approach, since then finite elements with vanishing stiffness occur, resulting in an unsolvable system of equations. To amend this issue, the $\nu(\boldsymbol{X}) = 0$ material points are assigned a small, but finite, stiffness $\delta_o > 0$ (cf. (4.4) and (4.5)), which is assumed to have negligible influence on the structural response. This approach has successfully allowed many linear elastic topology optimization problems to be solved. However, for certain optimization problems involving e.g. eigenvalue problems or finite strains, the nearly void regions might cause numerical issues.

When solving eigenvalue problems in topology optimization, the nearly void regions might yield artificial solutions (Pedersen (2000)). For example, if conducting vibration analyzes, the issue appears since the mass matrix scales linearly with ν, whereas the stiffness matrix scales non-linearly according to a penalization scheme, cf. (3.9). Accordingly, the stiffness-to-mass ratio becomes very small in regions wherein $\nu(\boldsymbol{X}) \ll 1$, which is readily verified by considering the Rayleigh quotient of (3.9), i.e.

$$\omega^2 = R(\boldsymbol{\phi}) := \frac{\boldsymbol{\phi}^T \mathsf{K} \boldsymbol{\phi}}{\boldsymbol{\phi}^T \mathsf{M} \boldsymbol{\phi}}. \tag{4.14}$$

In Fig. 4.2 the mass-to-stiffness SIMP and RAMP penalization ratios appear as a functions of ν for $p = \{1, ..., 8\}$, $q = \{1, ..., 8\}$ and $\delta_o = 10^{-3}$, cf. (4.4) and (4.5). The peaks appearing for the interpolations moves to the left and increases in amplitude as $\delta_o \to 0$. Clearly, any peak is unwanted, since it may give rise to artificial eigenmodes when ν takes on values in the vicinity of the peak.

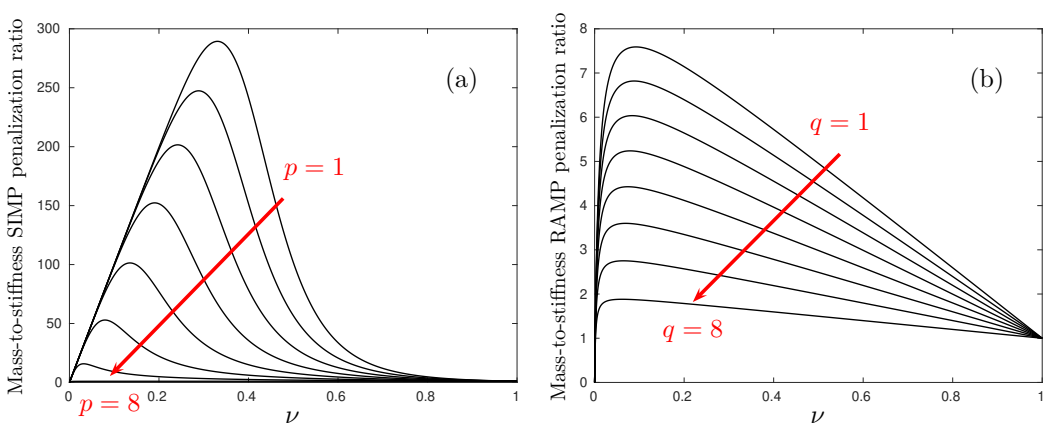

Fig. 4.2: The mass-to-stiffness penalization ratio versus ν for (a) SIMP and (b) RAMP. Here, $\delta_o = 10^{-3}$, cf. (4.4) and (4.5).

To mitigate the issue associated with the SIMP scheme, Du and Olhoff (2007) introduce a non-linear scaling of the mass for low ν values, such that the mass approaches zero faster than the stiffness.

Artificial solutions may also appear in the linearized buckling eigenvalue problem (3.18). In linear elastic analyzes, these solutions can be avoided by introducing different ν-scalings of K_o and K_g, similar to the aforementioned approaches involving K and M (cf. e.g. Gao and Ma (2015)). However, for non-linear hyperelasticity, $\mathsf{K} = \mathsf{K}_o + \mathsf{K}_g$ is the Hessian of the strain energy, and since the penalization is applied to the strain energy, K_o and K_g are penalized equally. Lindgaard and Dahl (2013) instead propose to use a larger δ_o, however at the cost of artificially stiff void regions. Gao and Ma (2015) distinguished between artificial and physical solutions via a strain energy density criterion, to the detriment of computational efficiency.

The fictitious domain approach to topology optimization might pose additional problems when void regions are subjected to finite deformations, as excessively distorted finite elements might result in loss of convergence in the iterative equilibrium iterations. To address this issue, Bruns and Tortorelli (2003) introduce a element removal method, such that elements wherein $\nu \to 0$ are removed from the analysis. Another approach is proposed by Wang et al. (2014), whereby the physical strain energy is replaced by a linearized strain energy in void region. In Papers A and B, it is shown that these methods also might mitigate the aforementioned issue of artificial eigenmodes in void regions.

4.3.1 Element removal

The element removal method introduced by Bruns and Tortorelli (2003) is able to both remove and reintroduce finite elements depending on the value of $\nu(\boldsymbol{X})$ within the elements, $\boldsymbol{X} \in \Omega^e$. Traditionally, the parametrization of the filtered design field ν is piece-wise constant over the finite elements or interpolated via the finite element shape functions to the quadrature points. In the latter approach, a measure of the mean design field ν_{mean} within a finite element Ω^e is computed. A small threshold $\varepsilon_r > 0$ then dictates the removal, $\nu_{mean} < \varepsilon_r$, or reintroduction, $\nu_{mean} > \varepsilon_r$, of the element. The main disadvantage of this method is its inherent non-differentiability, wherefore the gradient information provided to the optimizer will be discontinuous. However, the sensitivity information in void regions is often negligible, at least in the later stages of the optimization, wherefore a sufficiently small ε_r should mitigate such issues.

Ideally, the finite elements should be removed or reintroduced during the optimization without altering the predefined sparse patterns of the involved matrices. To this end, the assembly process is monitored such that if a finite element is marked for removal, its stiffness, mass and internal force contributions are set to zero. Subsequently, Dirichlet conditions are assigned to any "hanging" finite element nodes, i.e. nodes for which all neighbor elements are removed. In this way, the global stiffness matrix retains its positive definiteness.

Since the element removal method excludes nearly void regions from the equilibrium analysis, it also removes the associated degrees-of-freedom from the eigenspace, i.e. eliminates artificial eigenmodes. In Paper A, the success of this approach is proven for the topology optimization of eigenfrequency spectra of structures subject to finite deformations.

4.3.2 Energy transition

In the energy transition proposed by Wang et al. (2014), the physical strain energy density, W^{PH}, is weighted against the linearized energy, W^L, such that the strain energy density becomes

$$\begin{aligned} W(\gamma\boldsymbol{\nabla u}, \boldsymbol{\nabla u}) &= W^{PH}(\gamma\boldsymbol{\nabla u}) + W^L(\boldsymbol{\nabla u}) - W^L(\gamma\boldsymbol{\nabla u}) \\ &= W^{PH}(\gamma\boldsymbol{\nabla u}) + (1-\gamma^2)W^L(\boldsymbol{\nabla u}), \end{aligned} \tag{4.15}$$

where $\gamma : [0,1] \to [0,1]$ is

$$\gamma = H_{b,h}(\nu) = \frac{\tanh(bh) + \tanh(b(\nu^p - h))}{\tanh(bh) + \tanh(b(1-h))}, \tag{4.16}$$

and b, h are numerical parameters which dictate the shape of the approximative Heaviside step function $H_{b,h} : \mathbb{R} \to [0,1]$, cf. Wang et al. (2014). Accordingly, as $\nu \to 0$ also $\gamma \to 0$, wherefore the physical strain energy density is replaced by the linearized strain energy density. To continue, the deformation gradient is redefined as $\boldsymbol{F} = \mathbf{1} + \gamma\boldsymbol{\nabla u}$ and

$$\begin{aligned} \frac{\partial W}{\partial \boldsymbol{\nabla u}} : \boldsymbol{\nabla}\delta\boldsymbol{u} &= \frac{\partial W^{PH}}{\partial \gamma\boldsymbol{\nabla u}} : \gamma\boldsymbol{\nabla}\delta\boldsymbol{u} + (1-\gamma^2)\frac{\partial W^L}{\partial \boldsymbol{\nabla u}} : \boldsymbol{\nabla}\delta\boldsymbol{u} \\ &= \boldsymbol{P}^{PH} : \delta\boldsymbol{F} + (1-\gamma^2)\boldsymbol{\sigma}^L : \delta\boldsymbol{\epsilon}, \end{aligned} \tag{4.17}$$

replaces $\frac{\partial W}{\partial \boldsymbol{F}} : \delta\boldsymbol{F}$ in the weak form (cf. e.g. (2.3)) and $\boldsymbol{\sigma}^L$ is the linearized stress tensor.

In Paper B, the energy transition is used to eliminate artificial buckling modes in void regions. To understand its principle of action, let us consider the energy transition generated K_o and K_g stiffness matrices, which are obtained by discretizing and linearizing the weak form (2.3) with (4.17), i.e.

$$\begin{aligned} \mathsf{K}_o &= \sum\sum \int_{\Omega^e} \left(\gamma^2 \mathsf{k}_o^e + (1-\gamma^2)\mathsf{k}_l^e\right) \, dV, \\ \mathsf{K}_g &= \sum\sum \int_{\Omega^e} \gamma^2 \mathsf{k}_g^e \, dV, \end{aligned} \tag{4.18}$$

where k_o^e and k_g^e are the element versions of K_o and K_g, and k_l^e is the linear element stiffness matrix. The (3.18) eigenvalue problem thereby yields the Rayleigh quotient

$$\pi = R(\phi) = -\frac{\boldsymbol{\Phi}^T \mathsf{K}_o \boldsymbol{\Phi}}{\boldsymbol{\Phi}^T \mathsf{K}_g \boldsymbol{\Phi}} = -\frac{\boldsymbol{\Phi}^T \left(\sum\sum \int_{\Omega^e} \left(\gamma^2 \mathsf{k}_o^e + (1-\gamma^2)\mathsf{k}_l^e\right) \, dV\right) \boldsymbol{\Phi}}{\boldsymbol{\Phi}^T \left(\sum\sum \int_{\Omega^e} \gamma^2 \mathsf{k}_g^e \, dV\right) \boldsymbol{\Phi}}. \tag{4.19}$$

Indeed, the denominator of (4.19) tends to zero as $\gamma \to 0$, whereas the numerator tends to a finite value, wherefore the artificial eigenvalues should become large.

5 Future perspectives

There always exists a trade-off between structural *stiffness* and *strength*. This is evident when considering the maximum stiffness design, which often consists of tension/compression loaded slender members, where the compressive loads obviously threatens the structure's integrity due to buckling. Here, the approach in Paper B could be utilized to ensure that a safety factor against buckling exists at operating load conditions. However, even if a structure has high buckling strength, it might still fail due to yielding. It can therefore be argued that the definition of an stiffness optimal design must take all of these considerations into account. Recently, progress has been made towards this goal, however using simplifying linear assumptions (Wang et al. (2023), Andersen et al. (2022)). To take this further, an optimization framework which accurately models the yield and buckling strengths using elastoplasticity and instability analyzes should be developed.

It is however also important to remember that the prevention of instabilities must not always be the ultimate goal. For example, the review paper written by Kochmann and Bertoldi (2017), illustrate a wide range of examples wherein structures and materials which exhibit instabilities are utilized in order to obtain exotic structural properties. Often, these examples involve elastomeric materials, which can be modeled using hyperelastic or viscoelastic models depending on the rate at which they are loaded. Topology optimization has already been used to design systems utilizing instabilities. For example, a non-convex potential energy landscape is exploited in the systematic design of an energy dissipating system by Deng et al. (2020) and of bi-stable programmable structures by Wallin et al. (2021). There are however still many aspects to these design problems that are yet to be investigated, such as rate-dependent or dynamic effects and multi-scale instabilities.

Unfortunately, the accuracy in the characterization of many physical phenomena tends to be highly dependent upon the modeling of the design boundaries. Topology optimization is especially problematic in this regard, due to the smearing effect obtained in the filtering procedure. The issue is exemplified in Paper C for phononic bandgaps, and in Paper E for contact problems. To improve the boundary modeling, simultaneous shape and topology optimization could be utilized, an approach which is investigated in Paper E for pressure driven soft robots. In the future, this method should be developed and tested on various boundary sensitive optimization problems, involving effects such as fluid-solid interactions, acoustics and instabilities.

6 Summary of the appended papers

Paper A: An eigenfrequency constrained topology optimization framework which incorporates hyperelastic materials, nonlinear kinematics, and preloads is established. The method generates designs with maximized end-compliance at a given volume, which also fulfill a lower bound constraint on the lowest eigenfrequencies. The adjoint method typically employed in the sensitivity analysis is extended to simple and degenerate eigenfrequencies in the finite strain setting. Artificial eigenmodes are removed by utilizing an element removal scheme. Numerical examples illustrate that the magnitude of the eigenfrequencies depend significantly on the load level. Several designs with the desired fundamental eigenfrequency are presented.

Paper B: A strain energy transition approach is proposed to remove the artificial buckling modes that invariably occur when including structural stability in topology optimization problems. The structural and material response are assumed to be non-linear, wherefore a finite deformation hyperelastic simulation is conducted. The topology optimization aims to minimize the displacement of the design, subject to lower bound constraints on the lowest critical buckling loads and maximum volume. The critical buckling load levels are estimated by an eigenvalue analysis using the one point approach. The numerical examples show the effectiveness of the energy transition scheme in combination with the topology optimization.

Paper C: A topology optimization based inverse homogenization design framework of mechanically tunable phononic crystal materials is presented. The formulation is based on length scale separation, which allows the dispersion relations to be obtained by analyzing a single unit cell subjected to Floquet-Bloch boundary conditions. The dispersion properties are controlled by applying a finite macroscopic deformation to the unit cell. Several designs which exemplify the tuneability of the dispersion-deformation relation are obtained using the proposed method. A verifying post-processing analysis is conducted using a conforming finite element mesh.

Paper D: An inverse homogenization approach via topology optimization is used to design metamaterials with sought macroscopic stress-strain behaviors. Internal contact is allowed as a non-linear mechanism by a third medium contact method. Rigorous post-processing analyzes are conducted, in which conventional contact formulations are used in a commercial software. To further investigate the impact of the imprecise boundary modeling, a topology optimized design is used as initial design to a shape optimization.

Paper E: A simultaneous shape and topology optimization approach is established and applied to the design of pressure driven soft robots. The topology optimization is density based, and is used to design the general morphology of the robots. A regularized nodal based approach to shape optimization is applied to surfaces where the pressure load is applied. The motion of the robots is captured using a quasi-static hyperelastic framework, and the rubber-like nature of the involved elastomeric materials is modeled via mixed finite elements. Several designs of pressure driven soft robots are presented.

References

Aage, N., Andreassen, E., Lazarov, B.S., Sigmund, O., 2017. Giga-voxel computational morphogenesis for structural design. Nature 550, 84–86.

Alexandersen, J., Sigmund, O., Aage, N., 2016. Large scale three-dimensional topology optimisation of heat sinks cooled by natural convection. International Journal of Heat and Mass Transfer 100, 876–891.

Allaire, G., Jouve, F., Toader, A.M., 2002. A level-set method for shape optimization. Comptes Rendus Mathematique 334, 1125–1130.

Andersen, M.N., Wang, Y., Wang, F., Sigmund, O., 2022. Buckling and yield strength estimation of architected materials under arbitrary loads. International Journal of Solids and Structures 254, 111842.

Andreasen, C.S., Elingaard, M.O., Aage, N., 2020. Level set topology and shape optimization by density methods using cut elements with length scale control. Structural and Multidisciplinary Optimization 62, 685–707.

Bathe, K.J., 2006. Finite element procedures. Klaus-Jurgen Bathe.

Belegundu, A., Rajan, S., 1988. A shape optimization approach based on natural design variables and shape functions. Computer Methods in Applied Mechanics and Engineering 66, 87–106.

Bendsøe, M.P., 1989. Optimal shape design as a material distribution problem. Structural optimization 1, 193–202.

Bendsøe, M.P., Kikuchi, N., 1988. Generating optimal topologies in structural design using a homogenization method. Computer methods in applied mechanics and engineering 71, 197–224.

Bendsøe, M.P., Sigmund, O., 1999. Material interpolation schemes in topology optimization. Archive of applied mechanics 69, 635–654.

Bertoldi, K., Boyce, M., 2008. Mechanically triggered transformations of phononic band gaps in periodic elastomeric structures. Physical Review B 77, 052105.

Bertoldi, K., Reis, P.M., Willshaw, S., Mullin, T., 2010. Negative poisson's ratio behavior induced by an elastic instability. Advanced materials 22, 361–366.

Borrvall, T., Petersson, J., 2003. Topology optimization of fluids in stokes flow. International journal for numerical methods in fluids 41, 77–107.

Bourdin, B., 2001. Filters in topology optimization. International journal for numerical methods in engineering 50, 2143–2158.

Bourdin, B., Chambolle, A., 2003. Design-dependent loads in topology optimization. ESAIM: Control, Optimisation and Calculus of Variations 9, 19–48.

Braibant, V., Fleury, C., 1984. Shape optimal design using b-splines. Computer methods in applied mechanics and engineering 44, 247–267.

Brendel, B., Ramm, E., 1980. Linear and nonlinear stability analysis of cylindrical shells. Computers & structures 12, 549–558.

Bruns, T.E., Tortorelli, D.A., 2001. Topology optimization of non-linear elastic structures and compliant mechanisms. Computer methods in applied mechanics and engineering 190, 3443–3459.

Bruns, T.E., Tortorelli, D.A., 2003. An element removal and reintroduction strategy for the topology optimization of structures and compliant mechanisms. International journal for numerical methods in engineering 57, 1413–1430.

Buhl, T., Pedersen, C.B., Sigmund, O., 2000. Stiffness design of geometrically nonlinear structures using topology optimization. Structural and Multidisciplinary Optimization 19, 93–104.

Burman, E., Elfverson, D., Hansbo, P., Larson, M.G., Larsson, K., 2019. Cut topology optimization for linear elasticity with coupling to parametric nondesign domain regions. Computer Methods in Applied Mechanics and Engineering 350, 462–479.

Carstensen, J.V., Lotfi, R., Chen, W., Szyniszewski, S., Gaitanaros, S., Schroers, J., Guest, J.K., 2022. Topology-optimized bulk metallic glass cellular materials for energy absorption. Scripta Materialia 208, 114361.

Chenais, D., 1975. On the existence of a solution in a domain identification problem. Journal of Mathematical Analysis and Applications 52, 189–219.

Cheng, K.T., Olhoff, N., 1981. An investigation concerning optimal design of solid elastic plates. International Journal of Solids and Structures 17, 305–323.

Clausen, A., Andreassen, E., 2017. On filter boundary conditions in topology optimization. Structural and Multidisciplinary Optimization 56, 1147–1155.

Crisfield, M.A., 1993. Non-linear finite element analysis of solids and structures. volume 1. Wiley.

Dalklint, A., Wallin, M., Bertoldi, K., Tortorelli, D., 2022. Tunable phononic bandgap materials designed via topology optimization. Journal of the Mechanics and Physics of Solids 163, 104849.

Dalklint, A., Wallin, M., Tortorelli, D.A., 2020. Eigenfrequency constrained topology optimization of finite strain hyperelastic structures. Structural and Multidisciplinary Optimization 61, 2577–2594.

Dalklint, A., Wallin, M., Tortorelli, D.A., 2021. Structural stability and artificial buckling modes in topology optimization. Structural and Multidisciplinary Optimization 64, 1751–1763.

De Souza Neto, E.A., Blanco, P.J., Sánchez, P.J., Feijóo, R.A., 2015. An rve-based multiscale theory of solids with micro-scale inertia and body force effects. Mechanics of Materials 80, 136–144.

Deaton, J.D., Grandhi, R.V., 2014. A survey of structural and multidisciplinary continuum topology optimization: post 2000. Structural and Multidisciplinary Optimization 49, 1–38.

Deng, H., Cheng, L., Liang, X., Hayduke, D., To, A.C., 2020. Topology optimization for energy dissipation design of lattice structures through snap-through behavior. Computer Methods in Applied Mechanics and Engineering 358, 112641.

Du, J., Olhoff, N., 2007. Topological design of freely vibrating continuum structures for maximum values of simple and multiple eigenfrequencies and frequency gaps. Structural and Multidisciplinary Optimization 34, 91–110.

Dyck, D.N., Lowther, D.A., 1996. Automated design of magnetic devices by optimizing material distribution. IEEE Transactions on Magnetics 32, 1188–1193.

Florijn, B., Coulais, C., van Hecke, M., 2014. Programmable mechanical metamaterials. Physical review letters 113, 175503.

Frenzel, T., Findeisen, C., Kadic, M., Gumbsch, P., Wegener, M., 2016. Tailored buckling microlattices as reusable light-weight shock absorbers. Advanced Materials 28, 5865–5870.

Gao, X., Ma, H., 2015. Topology optimization of continuum structures under buckling constraints. Computers & Structures 157, 142–152.

Groen, J.P., Sigmund, O., 2018. Homogenization-based topology optimization for high-resolution manufacturable microstructures. International Journal for Numerical Methods in Engineering 113, 1148–1163.

Guest, J.K., Prévost, J.H., Belytschko, T., 2004. Achieving minimum length scale in topology optimization using nodal design variables and projection functions. International journal for numerical methods in engineering 61, 238–254.

Haber, R.B., Jog, C.S., Bendsøe, M.P., 1996. A new approach to variable-topology shape design using a constraint on perimeter. Structural optimization 11, 1–12.

Haftka, R.T., Grandhi, R.V., 1986. Structural shape optimization—a survey. Computer methods in applied mechanics and engineering 57, 91–106.

Hashin, Z., Shtrikman, S., 1963. A variational approach to the theory of the elastic behaviour of multiphase materials. Journal of the Mechanics and Physics of Solids 11, 127–140.

Hill, R., 1972. On constitutive macro-variables for heterogeneous solids at finite strain. Proceedings of the Royal Society of London. A. Mathematical and Physical Sciences 326, 131–147.

Holzapfel, G.A., 2002. Nonlinear solid mechanics: a continuum approach for engineering science. Meccanica 37, 489–490.

Ivarsson, N., Wallin, M., Tortorelli, D., 2018. Topology optimization of finite strain viscoplastic systems under transient loads. International Journal for Numerical Methods in Engineering 114, 1351–1367.

Jensen, J.S., 2003. Phononic band gaps and vibrations in one-and two-dimensional mass–spring structures. Journal of sound and Vibration 266, 1053–1078.

Jensen, J.S., Sigmund, O., 2011. Topology optimization for nano-photonics. Laser & Photonics Reviews 5, 308–321.

Joannopoulos, J.D., Johnson, S.G., Winn, J.N., Meade, R.D., 2011. Photonic crystals. Princeton university press.

Kang, Z., James, K.A., 2022. Multiphysics design of programmable shape-memory alloy-based smart structures via topology optimization. Structural and Multidisciplinary Optimization 65, 24.

Kemmler, R., Lipka, A., Ramm, E., 2005. Large deformations and stability in topology optimization. Structural and Multidisciplinary Optimization 30, 459–476.

Kittel, C., 1976. Introduction to solid state physics.

Kochmann, D.M., Bertoldi, K., 2017. Exploiting microstructural instabilities in solids and structures: from metamaterials to structural transitions. Applied mechanics reviews 69.

Larsen, U.D., Sigmund, O., Bouwsta, S., 1997. Design and fabrication of compliant micromechanisms and structures with negative poisson's ratio. Journal of microelectromechanical systems 6, 99–106.

Lazarov, B.S., Sigmund, O., 2011. Filters in topology optimization based on helmholtz-type differential equations. International Journal for Numerical Methods in Engineering 86, 765–781.

Le, C., Bruns, T., Tortorelli, D., 2011. A gradient-based, parameter-free approach to shape optimization. Computer Methods in Applied Mechanics and Engineering 200, 985–996.

Leon, S.E., Lages, E.N., De Araújo, C.N., Paulino, G.H., 2014. On the effect of constraint parameters on the generalized displacement control method. Mechanics Research Communications 56, 123–129.

Li, L., Zhang, G., Khandelwal, K., 2017. Topology optimization of energy absorbing structures with maximum damage constraint. International Journal for Numerical Methods in Engineering 112, 737–775.

Lindgaard, E., Dahl, J., 2013. On compliance and buckling objective functions in topology optimization of snap-through problems. Structural and Multidisciplinary Optimization 47, 409–421.

Makhija, D., Maute, K., 2014. Numerical instabilities in level set topology optimization with the extended finite element method. Structural and Multidisciplinary Optimization 49, 185–197.

Mandel, J., 1971. Plasticité classique et viscoplasticité (cism lecture notes, udine, italy).

Maurin, F., Claeys, C., Deckers, E., Desmet, W., 2018. Probability that a band-gap extremum is located on the irreducible brillouin-zone contour for the 17 different plane crystallographic lattices. International Journal of Solids and Structures 135, 26–36.

Maute, K., Ramm, E., 1995. Adaptive topology optimization. Structural optimization 10, 100–112.

Maute, K., Schwarz, S., Ramm, E., 1998. Adaptive topology optimization of elastoplastic structures. Structural optimization 15, 81–91.

Mhapsekar, K., McConaha, M., Anand, S., 2018. Additive manufacturing constraints in topology optimization for improved manufacturability. Journal of Manufacturing Science and Engineering 140.

Michell, A.G.M., 1904. Lviii. the limits of economy of material in frame-structures. The London, Edinburgh, and Dublin Philosophical Magazine and Journal of Science 8, 589–597.

Ogden, R.W., 2007. Incremental statics and dynamics of pre-stressed elastic materials. Waves in nonlinear pre-stressed materials , 1–26.

Pedersen, N.L., 2000. Maximization of eigenvalues using topology optimization. Structural and multidisciplinary optimization 20, 2–11.

Petersson, J., Sigmund, O., 1998. Slope constrained topology optimization. International Journal for Numerical Methods in Engineering 41, 1417–1434.

Rus, D., Tolley, M.T., 2015. Design, fabrication and control of soft robots. Nature 521, 467–475.

Sachs, G., 1928. Zur ableitung einer filebbedingung. Z-VDI 72, 734.

Saeb, S., Steinmann, P., Javili, A., 2016. Aspects of computational homogenization at finite deformations: a unifying review from reuss' to voigt's bound. Applied Mechanics Reviews 68.

Scherer, M., Denzer, R., Steinmann, P., 2010. A fictitious energy approach for shape optimization. International Journal for Numerical Methods in Engineering 82, 269–302.

Schleupen, A., Maute, K., Ramm, E., 2000. Adaptive fe-procedures in shape optimization. Structural and Multidisciplinary Optimization 19, 282–302.

Sigmund, O., 1994. Design of material structures using topology optimization. Ph.D. thesis. Technical University of Denmark Lyngby.

Sigmund, O., Maute, K., 2013. Topology optimization approaches: A comparative review. Structural and Multidisciplinary Optimization 48, 1031–1055.

Sigmund, O., Petersson, J., 1998. Numerical instabilities in topology optimization: a survey on procedures dealing with checkerboards, mesh-dependencies and local minima. Structural optimization 16, 68–75.

Sigmund, O., Søndergaard Jensen, J., 2003. Systematic design of phononic band–gap materials and structures by topology optimization. Philosophical Transactions of the Royal Society of London. Series A: Mathematical, Physical and Engineering Sciences 361, 1001–1019.

Sigmund, O., Torquato, S., 1997. Design of materials with extreme thermal expansion using a three-phase topology optimization method. Journal of the Mechanics and Physics of Solids 45, 1037–1067.

Sokolowski, J., Zochowski, A., 1999. On the topological derivative in shape optimization. SIAM journal on control and optimization 37, 1251–1272.

Stolpe, M., Svanberg, K., 2001. An alternative interpolation scheme for minimum compliance topology optimization. Structural and Multidisciplinary Optimization 22, 116–124.

Swartz, K., Mittal, K., Schmidt, M., Barrera, J., Watts, S., Tortorelli, D., 2023. Yet another parameter-free shape optimization method .

Taylor, G.I., 1938. Plastic strain in metals. J. Inst. Metals 62, 307–324.

Salazar de Troya, M.A., Tortorelli, D.A., 2018. Adaptive mesh refinement in stress-constrained topology optimization. Structural and Multidisciplinary Optimization 58, 2369–2386.

Villanueva, C.H., Maute, K., 2017. Cutfem topology optimization of 3d laminar incompressible flow problems. Computer Methods in Applied Mechanics and Engineering 320, 444–473.

Wallin, M., Dalklint, A., Tortorelli, D., 2021. Topology optimization of bistable elastic structures—an application to logic gates. Computer Methods in Applied Mechanics and Engineering 383, 113912.

Wallin, M., Ivarsson, N., Amir, O., Tortorelli, D., 2020. Consistent boundary conditions for pde filter regularization in topology optimization. Structural and Multidisciplinary Optimization 62, 1299–1311.

Wallin, M., Ivarsson, N., Ristinmaa, M., 2015. Large strain phase-field-based multi-material topology optimization. International Journal for Numerical Methods in Engineering 104, 887–904.

Wallin, M., Ivarsson, N., Tortorelli, D., 2018. Stiffness optimization of non-linear elastic structures. Computer Methods in Applied Mechanics and Engineering 330, 292–307.

Wallin, M., Ristinmaa, M., Askfelt, H., 2012. Optimal topologies derived from a phase-field method. Structural and Multidisciplinary Optimization 45, 171–183.

Wallin, M., Tortorelli, D.A., 2020. Nonlinear homogenization for topology optimization. Mechanics of Materials 145, 103324.

Wang, F., 2018. Systematic design of 3d auxetic lattice materials with programmable poisson's ratio for finite strains. Journal of the Mechanics and Physics of Solids 114, 303–318.

Wang, F., Brøns, M., Sigmund, O., 2023. Non-hierarchical architected materials with extreme stiffness and strength. Advanced Functional Materials , 2211561.

Wang, F., Lazarov, B.S., Sigmund, O., Jensen, J.S., 2014. Interpolation scheme for fictitious domain techniques and topology optimization of finite strain elastic problems. Computer Methods in Applied Mechanics and Engineering 276, 453–472.

Wang, M.Y., Wang, X., Guo, D., 2003. A level set method for structural topology optimization. Computer methods in applied mechanics and engineering 192, 227–246.

Wriggers, P., 2008. Nonlinear finite element methods. Springer Science & Business Media.

Xia, Q., Shi, T., Liu, S., Wang, M.Y., 2012. A level set solution to the stress-based structural shape and topology optimization. Computers & Structures 90, 55–64.

Yoon, G.H., 2010a. Maximizing the fundamental eigenfrequency of geometrically nonlinear structures by topology optimization based on element connectivity parameterization. Computers & structures 88, 120–133.

Yoon, G.H., 2010b. Topology optimization for stationary fluid–structure interaction problems using a new monolithic formulation. International journal for numerical methods in engineering 82, 591–616.

Zhang, G., Feng, N., Khandelwal, K., 2021. A computational framework for homogenization and multiscale stability analyses of nonlinear periodic materials. International Journal for Numerical Methods in Engineering 122, 6527–6575.

Zhang, G., Khandelwal, K., 2020. Topology optimization of dissipative metamaterials at finite strains based on nonlinear homogenization. Structural and Multidisciplinary Optimization 62, 1419–1455.

Zhang, K., Cheng, G., 2020. Three-dimensional high resolution topology optimization considering additive manufacturing constraints. Additive Manufacturing 35, 101224.

Zhang, P., Parnell, W.J., 2017. Soft phononic crystals with deformation-independent band gaps. Proceedings of the Royal Society A: Mathematical, Physical and Engineering Sciences 473, 20160865.

Zhao, Z., Zhang, X.S., 2022. Topology optimization of hard-magnetic soft materials. Journal of the Mechanics and Physics of Solids 158, 104628.

Zienkiewicz, O., Campbell, J., 1973. Shape optimization and sequential linear programming in optimum structural design. John Wily, NewYork .